

Spontaneous Symmetry Breaking for Extreme Vorticity and Strain in the 3D Navier-Stokes Equations

Timo Schorlepp,^{1,*} Tobias Grafke,² Sandra May,³ and Rainer Grauer¹

¹*Institute for Theoretical Physics I, Ruhr-University Bochum,
Universitätsstrasse 150, 44801 Bochum, Germany*

²*Mathematics Institute, University of Warwick, Coventry CV4 7AL, United Kingdom*

³*Department of Mathematics, TU Dortmund University,
Vogelpothsweg 87, 44227 Dortmund, Germany*

(Dated: April 4, 2022)

We investigate the spatio-temporal structure of the most likely configurations realising extremely high vorticity or strain in the stochastically forced 3D incompressible Navier-Stokes equations. Most likely configurations are computed by numerically finding the highest probability velocity field realising an extreme constraint as solution of a large optimisation problem. High-vorticity configurations are identified as pinched vortex filaments with swirl, while high-strain configurations correspond to counter-rotating vortex rings. We additionally observe that the most likely configurations for vorticity and strain spontaneously break their rotational symmetry for extremely high observable values. Instanton calculus and large deviation theory allow us to show that these maximum likelihood realisations determine the tail probabilities of the observed quantities. In particular, we are able to demonstrate that artificially enforcing rotational symmetry for large strain configurations leads to a severe underestimate of their probability, as it is dominated in likelihood by an exponentially more likely symmetry broken vortex-sheet configuration.

Keywords: Large deviation theory, instantons, extreme events, optimal control, Navier-Stokes turbulence, vortex sheets

CONTENTS

I. Introduction and Motivation	2
II. Instantons for the 3D Navier-Stokes equations	3
1. Stochastic action and minimisers	3
2. Instanton equations for Navier-Stokes with axisymmetric observables	5
3. Numerical procedure	6
III. Results	7
1. Extreme vorticity events	7
2. Extreme strain events	8
3. Extreme event probabilities	9
IV. Conclusion	11
Acknowledgments	12
Appendix: Supplemental material	12
A. Introduction and Outline	12
1. Setup of the problem	12
2. Reformulation as an optimal control problem	13
B. Conversion to unconstrained problems	14
1. Method of Lagrange multipliers	14
2. Penalty method	15
3. Augmented Lagrangian method	15
C. Gradient-based minimisation: Gradient descent and L-BFGS method	16
1. Instanton equations	16
2. Adjoint state method	17
3. Minimisation algorithms – Gradient descent	18
4. Minimisation algorithms – L-BFGS method	20
5. Memory reduction techniques	21

* Timo.Schorlepp@rub.de

D. Three-dimensional Navier-Stokes instanton implementation	23
1. Derivation of the adjoint equation	23
2. Forcing	25
3. Observables and final conditions for the adjoint field	26
4. Numerical implementation and parameters	27
E. Axisymmetric Navier-Stokes instanton implementation	27
1. Axisymmetric instanton equations and boundary conditions	28
2. Spatio-temporal discretisation	29
3. Fast evaluation of polar convolutions	30
4. Numerical implementation and parameters	32
References	33

I. INTRODUCTION AND MOTIVATION

Turbulence is characterised by its tendency to intermittently dissipate energy in very localised and intense events. These extreme events dominate the statistics of quantities such as high order structure functions, and are ultimately responsible for the anomalous scaling of fully developed turbulent flows. It is generally believed that short bursts of intense vortex stretching are the mechanism for the formation of these events.

Taking this as starting point, in this paper we address the question: What structures are naturally generated in the 3D incompressible Navier-Stokes equations (NSE) to realise events of extreme vortex stretching, strain production and energy dissipation? For this, we are concentrating on small-scale structures that lead to extreme values of the fluid vorticity or its strain. Concretely, we set out to compute the most likely configuration (for a given large-scale stochastic forcing) that realises a large vorticity or strain value at a single point within the domain, at an instantaneous moment in time, and how the velocity field configuration around this point facilitates the extreme burst.

This question has been discussed in the literature, starting with Novikov [1, 2], and more recent works that explored extreme vorticity and strain events in very large turbulent simulations [3, 4]. These attempts, which solely rely on brute-force direct numerical simulations (DNS), have the intrinsic complication that any extreme realisation of an observable will necessarily be very rare, and thus hard to observe. Therefore, exploring extreme events not only requires high numerical resolution, but further extremely large data-sets, most of which are wasted because they do not exhibit the desired event. On this basis, we instead employ specific rare event techniques [5], in particular stochastic field theory and instanton calculus [6], or equivalently, sample path large deviation theory [7]. The two are intimately connected [6, 8], and have proven successful in related fields, such as extreme shocks in Burgers turbulence [9–11], extreme surface heights in the Kardar-Parisi-Zhang (KPZ) equation [12], in ocean waves and tsunamis [13, 14], or extreme mechanical forces in grid-generated turbulence [15]. The key idea is to replace the inefficient naive sampling approach by a deterministic optimisation problem that yields the maximum likelihood trajectory of the system that leads to a prescribed rare outcome. The advantage of this method is the fact that it yields the best estimate of the *typical* extreme event in the limit of it becoming increasingly rare, which is the limit we are most interested in, and at the same time also the regime that is hardest to reach via DNS.

As we will discuss later, instanton techniques not only allow for the computation of the limiting most likely path to obtain an extreme event, but further yield estimates for the exponential tail scaling of the observable’s probability density function (PDF). A concrete prediction of our results is the fact that intuitive rotationally symmetric realisations of extreme vorticity outcomes (namely, vortex tubes/filaments) or extreme strain outcomes (namely, colliding or contracting vortex rings) are not necessarily the most likely way to reach extreme values, even if the observable exhibits rotational symmetry. In fact we present that the rotationally symmetric events become subdominant, particularly for large positive strain values, and are dominated in probability by asymmetric field configurations. In other words, the stochastic instanton undergoes spontaneous symmetry breaking, and the corresponding action exhibits a dynamical phase transition similar to what is observed e.g. in the KPZ equation [16].

This paper is organised as follows: We discuss the instanton approach, as applied to the NSE, in section II by first introducing the instanton formalism in section II 1 in general and subsequently applying it to the NSE in section II 2, where we also explain our conditioning on vorticity and strain. The numerical implementation of the corresponding optimisation problem is discussed in section II 3. In section III 1 we show the most likely configuration for extreme vorticity events as obtained by the numerical solution of the instanton problem. Section III 2 presents analogous results for extreme strain events. We will discuss the implication of these results on the likelihood and PDF tail scaling in section III 3 and then conclude with section IV. The supplemental material of this paper includes additional, detailed information on the numerical optimisation methods that have been used to generate the results of this paper.

II. INSTANTONS FOR THE 3D NAVIER-STOKES EQUATIONS

The 3D incompressible NSE on a domain $\Omega \subset \mathbb{R}^3$, given by

$$\begin{cases} \partial_t u + (u \cdot \nabla) u = -\nabla P + \nu \Delta u + \eta, \\ \nabla \cdot u = 0, \\ u(\cdot, -T) = u_0, \end{cases} \quad (1)$$

describe the spatio-temporal evolution of a velocity field $u : \Omega \times [-T, 0] \mapsto \mathbb{R}^3$, where $P(x, t)$ is the pressure field, $\eta(x, t)$ is the stochastic forcing term, $\nu > 0$ is the kinematic viscosity and u_0 is a deterministic initial condition. We restrict ourselves to a periodic domain $\Omega = [0, l]^3$, and consider a white-in-time, spatially stationary and solenoidal Gaussian forcing acting only on large scales as specified by the spatial covariance $\chi : \Omega \rightarrow \mathbb{R}^{3 \times 3}$:

$$\langle \eta(x, t) \eta^\top(x', t') \rangle = \chi(x - x') \delta(t - t'). \quad (2)$$

Additionally requiring the forcing to be statistically isotropic reduces the possible forms of χ to [17]

$$\chi(x) = f(\|x\|) \text{Id} + \frac{1}{2} \|x\| f'(\|x\|) \left[\text{Id} - \frac{xx^\top}{\|x\|^2} \right], \quad (3)$$

where $\text{Id} \in \mathbb{R}^{3 \times 3}$ denotes the identity matrix on \mathbb{R}^3 , and $f : [0, \infty) \rightarrow \mathbb{R}$ is an arbitrary function, which we choose as

$$f(r) = \chi_0 \exp \left\{ -\frac{r^2}{2\lambda^2} \right\} \quad (4)$$

for simplicity, with a correlation length λ of the order of the domain size l .

Extreme events in the NSE have been explored extensively in the literature. Particularly worth mentioning in connection with the instanton calculus is the work of Novikov et al. [1, 2]. They considered the conditionally averaged vorticity field, i.e. the average realisation of the vorticity field conditioned on a specific outcome of vorticity $\omega(x, t = 0)$ at a given point x . These fields, parametrised by ω , were obtained by performing many DNS, and averaging conditioned on the intended outcome. This procedure is closely related to the filtering approach [18] discussed in section III 1 and demonstrates the relevance of instanton solutions in real flows.

The structure of instanton solutions is of particular importance. As an example serves the observation that the rotational symmetric vorticity instanton in the two-dimensional NSE has no relevance at all [19]. Only taking into account symmetry breaking angle dependent contributions results in an effective action suitable for the instanton calculus.

In the case of the KPZ equation, symmetry breaking (or dynamical phase transition) has been demonstrated as the mechanism to generate the relevant instanton for obtaining the correct tail asymptotics [16]. Here, we make similar observations: symmetry breaking is essential to compute the relevant instanton with a pancake or sheet like structure (see figures 1 and 3). Whether these structures are related to the recently discovered confined vortex surfaces [20] and the tangential discontinuity of vortex sheets [21] poses a challenging question.

1. Stochastic action and minimisers

In this section, we briefly and formally introduce the instanton formalism for stochastic partial differential equations (SPDE) and comment on the applicability of the method in the context of Navier-Stokes turbulence to compute maximum likelihood space-time realisations of extreme events. For a generic SPDE for $u : \Omega \times [-T, 0] \rightarrow \mathbb{R}^3$

$$\begin{cases} \partial_t u(x, t) + N(u(\cdot, t))(x) = \sqrt{\varepsilon} \eta(x, t), \\ u(\cdot, -T) = u_0, \end{cases} \quad (5)$$

with a Gaussian forcing correlated according to (2) and noise strength $\varepsilon > 0$, expectations of a functional F with respect to the process u can formally be computed as a path integral

$$\langle F[u] \rangle = \int D\eta F[u[\eta]] e^{-\frac{1}{2\varepsilon} \int_{-T}^0 (\eta, \chi^{-1} * \eta)_{L^2(\Omega, \mathbb{R}^3)} dt} = \int_{u(\cdot, -T) = u_0} Du F[u] J[u] e^{-\frac{1}{\varepsilon} S[u]}, \quad (6)$$

where $*$ denotes spatial convolution and χ^{-1} is the convolutional inverse of the forcing correlation function χ . The Jacobian $J[u]$ is given by $J[u] = \exp\left\{\frac{1}{2} \int_{-T}^0 \text{tr} \nabla N(u) dt\right\}$ and S is the classical Onsager-Machlup [22] or Freidlin-Wentzell [7] action functional

$$S[u] = \int_{-T}^0 \mathcal{L}(u, \partial_t u) dt = \frac{1}{2} \int_{-T}^0 (\partial_t u + N(u), \chi^{-1} * [\partial_t u + N(u)])_{L^2(\Omega, \mathbb{R}^3)} dt \quad (7)$$

of the process u . In the case of a degenerate forcing, as in our specific application, we set $S[u] = +\infty$ if the trajectory does not lie in the image of the spatial convolution with χ . Suppose now that we are interested in evaluating the probability of measuring particular values of an *observable* O of the final time configuration $u(\cdot, t=0)$ in a subset $A \subset \mathbb{R}$. Then, in the small noise limit $\varepsilon \rightarrow 0$, the conditional path density and the probability will be dominated by the least unlikely path, in the sense that

$$P(O[u(\cdot, 0)] \in A) = \langle 1_{\{O[u(\cdot, 0)] \in A\}} \rangle \stackrel{\varepsilon \rightarrow 0}{\asymp} \exp \left\{ -\frac{1}{\varepsilon} \inf_{\substack{\tilde{u}(\cdot, -T) = u_0 \\ O[\tilde{u}(\cdot, 0)] \in A}} S[\tilde{u}] \right\}, \quad (8)$$

where $1_{\{\cdot\}}$ denotes the indicator function and “ \asymp ” stands for log-asymptotic equivalence (i.e. the logarithms of both sides are equal up to first order [23]). This follows formally by applying Laplace’s method to the path integral (6), or more rigorously by Freidlin-Wentzell theory [7]. We denote by u_1 the field configuration for which the functional S attains its global minimum for the given boundary conditions, i.e., u_1 solves the following minimisation problem:

$$\begin{cases} \min_u S[u], \\ \text{subject to } u(\cdot, -T) = u_0, \\ O[u(\cdot, 0)] \in A. \end{cases} \quad (9)$$

We call u_1 the *instanton* and $S_1 = S[u_1]$ the instanton action, and can thus gain access to limiting estimates of probabilities or probability density functions (PDFs) in the small noise limit $\varepsilon \rightarrow 0$ by solving the *deterministic* optimisation problem of finding u_1 via (9). For the estimation of PDFs $\rho_O(a)$, the target set is $A = [a, a + da]$ and hence the optimal field configuration is sought by minimising the action functional $S[u]$ subject to the constraint $O[u(\cdot, 0)] = a$, which is equivalent to maximizing its probability in path space. Introducing $p = \chi^{-1} * [\partial_t u + N(u)]$, we can reformulate (9) as a the minimisation problem with respect to p given by

$$\begin{cases} \min_p S[p] = \min_p \frac{1}{2} \int_{-T}^0 (p, \chi * p)_{L^2(\Omega, \mathbb{R}^3)} dt, \\ \text{subject to } \partial_t u + N(u) = \chi * p, \\ u(\cdot, -T) = u_0, \\ O[u(\cdot, 0)] = a, \end{cases} \quad (10)$$

with $u = u[p]$ being a function of the control p that is given by solving the PDE $\partial_t u + N(u) = \chi * p$, $u(\cdot, -T) = u_0$, forward in time.

We denote by p_1 the optimal control and by $u_1 = u[p_1]$ the associated optimal state. Then, the necessary optimality conditions for (10) (derived by using a formal Lagrange approach and eliminating the adjoint state variable afterwards, compare section C 1 in the supplemental material) yield the instanton equations

$$\begin{cases} \partial_t u_1 + N(u_1) = \chi * p_1, \\ \partial_t p_1 - (\nabla N(u_1))^\top p_1 = 0, \\ u_1(\cdot, -T) = u_0, \quad O[u_1(\cdot, 0)] = a, \\ p_1(\cdot, 0) = -\left. \frac{\delta O}{\delta u} \right|_{u_1(0)} \mathcal{F}_1. \end{cases} \quad (11)$$

Here, \mathcal{F}_1 is a Lagrange multiplier to enforce the final time constraint.

Note that we started our considerations by expressing the probability of an event via a path integral. The final object we obtain though, namely the instanton, is interesting in its own right in that it is exactly the *most likely* realisation of the outcome we set out to observe, regardless of whether it indeed represents the *typical* realisation of that outcome. The crucial subtlety here is that for a common event there are usually a multitude of possible histories for its creation, while an extreme outlier event is usually driven by a very specific and reproducible chain of events. The *average* field configuration realising a moderate vorticity, say, will in general be very different from its *most likely* configuration, and in fact is rather meaningless, as it averages over many different and unrelated physical mechanisms. For *extreme* events, on the other hand, the two notions coincide, and the most likely conditioned configuration precisely corresponds to the conditioned field average.

The connection to Freidlin-Wentzell theory [7] and large deviation theory rare events algorithms [8] allows us to make this notion rather precise: The large deviation limit in the setup that was outlined above is correct in the small noise limit. Through a suitable rescaling of (1), this limit is, in the first instance, equivalent to the low Reynolds number limit for the NSE: Non-dimensionalising all variables via $\tilde{x} = x/x_0$, $\tilde{t} = t/t_0$, $\tilde{u} = ut_0/x_0$, $\tilde{P} = Pt_0^2/x_0^2$ and $\tilde{\eta} = \eta t_0^{1/2}/\chi_0^{1/2}$ and choosing $t_0 = x_0^2/\nu$ yields

$$\begin{cases} \partial_t u + (u \cdot \nabla)u = -\nabla P + \Delta u + \sqrt{\varepsilon}\eta, \\ \nabla \cdot u = 0, \\ u(\cdot, -T) = u_0, \end{cases} \quad (12)$$

in the new variables. Here, $\varepsilon = \chi_0 x_0^4 \nu^{-3} = \text{Re}^3$ if x_0 is taken to be the characteristic length scale of the forcing and the characteristic velocity u_0 for the Reynolds number $\text{Re} = u_0 x_0/\nu$ is chosen as $u_0 = (\chi_0 x_0)^{1/3}$. This shows that as $\text{Re} \rightarrow 0$, the instanton prediction for quantities such as $\rho_O(a)$ will become asymptotically exact for the full range of the PDF. In contrast to this setup, we are interested in flows at a given and possibly large Reynolds number. This can be achieved by realising that the small noise (small Re) limit can be exchanged for an extreme event limit (see remark 1 in [24]): If the length and time scales are chosen such that $\varepsilon = \chi_0/(\nu a_0^2)$, and we focus on an event with $|O[u(\cdot, 0)]| = a_0 \gg \sqrt{\chi_0/\nu}$ (for an observable with dimension velocity over length), for a given Reynolds number, the instanton estimate for the typical event itself and its probability will be accurate for sufficiently large a_0 or sufficiently extreme events. For high Re , these observables must take very extreme values for the scaling limit to apply, making it very hard to observe in DNS. As a consequence and as we will confirm numerically in section III, the instanton scaling is readily reached for small Reynolds numbers, while it is entirely out of reach of direct sampling for high Re , because we are probing the tail scaling for extremely unlikely events. This associates instantons with structures deep within the dissipation range. We remark that the formation of these nearly singular dissipative structures (see sections III 1 and III 2) might be the cause of the dissipation anomaly [25].

2. Instanton equations for Navier-Stokes with axisymmetric observables

For the NSE (12), the instanton equations (11) can be written as

$$\begin{cases} \partial_t u_1 + \mathbb{P}[(u_1 \cdot \nabla)u_1] - \Delta u_1 = \chi * p_1, \\ \partial_t p_1 + \mathbb{P}[(u_1 \cdot \nabla)p_1 + (\nabla p_1)^\top u_1] + \Delta p_1 = 0, \\ u_1(\cdot, -T) = u_0, \quad O[u_1(\cdot, 0)] = a, \\ p_1(\cdot, 0) = -\mathbb{P}\left[\frac{\delta O}{\delta u}^\top \Big|_{u_1(0)} \mathcal{F}_1\right] \end{cases} \quad (13)$$

in coordinate-free form with $\nabla \cdot u_1 = \nabla \cdot p_1 = 0$. Here, the Leray projection $\mathbb{P} = \text{Id} - \nabla \Delta^{-1} \nabla \cdot$ onto the divergence-free part of a vector field [26] has been introduced in order to eliminate the pressure from the equations of motion and conveniently handle the incompressibility constraint within the general framework that has been presented in the previous section. A detailed derivation of (13) is carried out in section D 1 of the supplemental material.

We note that it is very challenging to make mathematically rigorous statements about the (unique) solvability of the corresponding minimisation problem (10) for the NSE, as well as about the question of local versus global solutions. We do not attempt to do this here. Instead, for assessing the validity of our results, we rely on the following observations: i) For the simplified case of the heat equation, the equation for p in (13) is independent of u and the instanton equations can be solved directly without an iterative procedure and thus that problem has a unique global minimiser; ii) For the NSE, we can get a good indication whether a numerically found solution to the minimisation problem is indeed globally optimal by comparing with the PDF as obtained via DNS; iii) For the NSE, we numerically validated our claim concerning the global optimality by restarting our optimisation algorithms at various points. Within this reasoning, we will assume in the numerical results that we have found globally optimal solutions.

We are interested in extreme events for two distinct one-dimensional observables: the vorticity $O_1[u(\cdot, 0)] = (\nabla \times u)_z(0, 0) = \omega_z(0, 0)$, and the strain $O_2[u(\cdot, 0)] = \partial_z u_z(0, 0)$. These observables correspond to the transversal and longitudinal components, respectively, of the velocity gradient tensor. Due to statistical isotropy and spatial stationarity, we are free to choose the respective z components as observables, as well as the origin $x = 0$ as the arbitrary point where the observables are evaluated.

Both observables naturally define a distinguished axis, around which the problem is rotationally symmetric. In particular, not only are the NSE rotationally symmetric, but also their corresponding action *including the conditioning on the observable* is invariant under rotation around this axis. It is therefore intuitive to search for a rotationally symmetric minimiser, and this is indeed also the nature of the structures that immediately come to mind for vorticity and strain: Strong vorticity will be observed at the core of a

particularly strong vortex filament, while large strain occurs at points such as the centre of the collision of two vortex rings. Of course it is not necessarily true that a rotationally symmetric optimisation problem has a rotationally symmetric minimiser.

Because of this fact, we set out to search for multiple, possibly distinct minimisers of the action: One for which we artificially enforce rotational symmetry, and potentially others for which no symmetry is enforced. The former case reduces the problem to (2+1) dimensions in (r, z, t) for cylindrical coordinates (r, θ, z) in space. In this coordinate system, and using the vorticity-streamfunction formulation for axisymmetric flows [27], the *axisymmetric* instanton equations are

$$\begin{cases} D_t u_\theta + \frac{1}{r} u_r u_\theta - L u_\theta = [\chi * p]_\theta, \\ D_t \omega_\theta - \frac{1}{r} u_r \omega_\theta - \frac{1}{r} \partial_z (u_\theta^2) - L \omega_\theta = [(\nabla \times \chi) * p]_\theta, \\ D_t p_\theta + \frac{1}{r} (2u_\theta p_r - u_r p_\theta) + L p_\theta = 0, \\ D_t \sigma_\theta - \frac{1}{r} \partial_z (u_\theta p_\theta) + \partial_z u_\theta \partial_r p_\theta - \partial_r u_\theta \partial_z p_\theta \\ \quad + 2(\omega_\theta + 2\partial_r u_z) \partial_r p_r + \frac{2}{r} \partial_r u_z p_r + (2\partial_z u_z + \frac{u_r}{r}) (2\partial_z p_r - \sigma_\theta) + L \sigma_\theta = 0, \end{cases} \quad (14)$$

where $D_t = \partial_t + u_r \partial_r + u_z \partial_z$ is the axisymmetric convective derivative, $L = \frac{1}{r} \partial_r (r \partial_r) - \frac{1}{r^2} + \partial_{zz}$ is an elliptic operator stemming from the vector Laplacian in cylindrical coordinates, and $\sigma = \nabla \times p$ is the vorticity of the adjoint field. In this formulation, the r and z components of the fields are reconstructed by solving $L\psi = -\omega_\theta$ for the streamfunction ψ and computing $u_r = -\partial_z \psi$ and $u_z = \frac{1}{r} \partial_r (r\psi)$.

The derivation of (14), as well as the spatio-temporal boundary conditions of the axisymmetric instanton fields, can be found in section E 1 of the supplemental material.

3. Numerical procedure

We consider the problem of minimising the action functional $S[u]$ given by (7) subject to a final time constraint $O[u(\cdot, 0)] = a \in \mathbb{R}$. Here, we briefly outline the numerical procedure that we use to compute axisymmetric and fully three-dimensional solutions.

We interpret the minimisation problem within the framework of PDE-constrained optimal control (see e.g. [28, 29]): We introduce the control variable p as discussed above and consider the optimisation problem (10). This is an optimal control problem with distributed control as the control p enters the PDE on the right hand side as a source term. The velocity field $u = u[p]$ corresponds to the state variable. By treating u as a function of p , we can follow the so-called reduced approach in optimal control theory and view the optimal control problem as a problem of the argument p only. We can recast (10) into a sequence of unconstrained optimisation problems using the augmented Lagrangian method [30]: For a sequence of positive penalty parameters $(\mu^{(m)})$ with $\mu^{(m)} \rightarrow \infty$ we minimise

$$L_A[p, \mathcal{F}, \mu] = S[p] + \mathcal{F} (O[u[p](\cdot, 0)] - a) + \frac{\mu}{2} (O[u[p](\cdot, 0)] - a)^2, \quad (15)$$

while updating the Lagrange multiplier \mathcal{F} via $\mathcal{F}^{(m+1)} = \mathcal{F}^{(m)} + \mu^{(m)} (O[u[p^{(m)}](\cdot, 0)] - a)$.

In other words, for each penalty parameter $\mu^{(m)}$, we need to solve a minimization problem, which in turn requires an iterative scheme. The computational costs can be reduced by using warm starts. This procedure allows us to compute instantons for a specified observable value a . This is in contrast to the optimisation approach by Chernykh and Stepanov [10] and others. There, the instanton equations, compare (11) for a generic SPDE, are solved by an iterative procedure during which the Lagrange multiplier \mathcal{F} is kept fixed and the value of a is allowed to change. This again produces a solution to the instanton equations, including a matching pair (\mathcal{F}, a) , but the value of a is not known a priori. This practical approach is convenient and computationally cheaper if there is a bijective map between \mathcal{F} and a and one is interested in solving the instanton equations over a wide range of values of a . Our approach is more general and to be preferred if i) there are multiple local minimisers, and the map $\mathcal{F} \mapsto a$ becomes multivalued, and ii) there are observable regions where the action fails to be convex and the \mathcal{F} - a -duality breaks down [31].

To minimise (15) for a given value $\mu^{(m)}$, we employ gradient based methods. As an improvement over a simple gradient descent (which, preconditioned with χ^{-1} , reduces to an iterative, fixed-point like solution of the instanton equations), we use the L-BFGS algorithm (see e.g. [32]). This significantly speeds up the computation for the fully three-dimensional instantons. The L-BFGS scheme is a limited-memory variant of one of the most popular quasi-Newton schemes, the BFGS scheme, named after Broyden, Fletcher, Goldfarb and Shanno. Quasi-Newton schemes only require gradient information (in contrast to the second-order derivative information needed for Newton) and typically show super-linear convergence (whereas the gradient scheme only converges linearly with rates that are often very close to 1 for ill-conditioned problems). Appropriate step sizes for the optimisation algorithm are determined by an Armijo line search using backtracking [32]. This very popular condition guarantees sufficient decrease that is proportional

to the step length. For the evaluation of the gradient, we use an adjoint approach: the gradient is given as $\delta L_A / \delta p = \chi * (p - z)$, where the adjoint state z solves the backward equation $\partial_t z - (\nabla N(u[p]))^\top z = 0$ with final condition $z(\cdot, 0) = -(\delta O / \delta u|_{u[p](\cdot, 0)})^\top (\mathcal{F} + \mu(O[u[p](\cdot, 0)] - a))$. Thus, each gradient evaluation requires to solve a PDE forward in time to determine $u[p]$ and then backwards to compute z . All of this is described in detail in section C in the supplemental material.

We use two different flow solvers within the described optimisation framework: a (2+1)-dimensional axisymmetric code as well as a (3+1)-dimensional code for the full problem. The (2+1)-dimensional code is necessary to compute solutions of the minimisation problem under the additional constraint of preserving axisymmetry. For the (3+1)-dimensional code, the rotationally symmetric instanton eventually ceases to be a local minimiser of the action as there are unstable directions that break symmetry. Symmetrisation stabilises the configurations and allows us to get access to the associated action. In other words, after symmetry breaking, the axisymmetric configuration ceases to be a minimiser of the full optimisation problem, but remains a (local) minimiser of the axisymmetric optimisation problem. The axisymmetric code is based on [33]: We use a Leapfrog scheme in time and symmetric second order finite differences on a regular r - z -grid in space, with a resolution of $n_t = 1024$ and $n_r = n_z = 256$. The diffusion term is discretised semi-implicitly to avoid a severe CFL constraint. Consequently, in each time step, we need to solve a Helmholtz-like equation to update the fields, for which we use a multigrid algorithm (see e.g. [34]). The polar convolutions with χ are evaluated by means of fast Hankel transforms [35, 36].

The full (3+1)-dimensional flow solver uses a pseudo-spectral method in space and the Heun scheme in time, with an integrating factor for the diffusion term. Thus, we again avoid a strict CFL constraint. We run a resolution of $n_t = 512$ and $n_x = n_y = n_z = 128$. For speed up, we implemented this on a GPU using the CUDA API. To fit a full (3+1)-dimensional optimisation problem on a single GPU, memory reduction techniques as described in [37] were necessary.

III. RESULTS

In the following, we show the outcome of our numerical computations, beginning with the instanton configurations before and after symmetry breaking for both vorticity and strain. We then discuss implications on the tail scaling of the PDFs, in particular for large positive strain.

1. Extreme vorticity events

Selecting $\omega_z(0,0) = a$ as our observable, we use the above formalism to numerically solve the optimisation problem (9). The result is the most likely configuration to realise an extreme vorticity outcome at final time. Note that this computation is independent of the choice of the Reynolds number. The Reynolds number, or equivalently ε , only determines whether a chosen observable a is rare, and thus whether the instanton formalism has any relevance for events of this size. As shown in figure 1, the most likely configuration to realise an extreme vorticity corresponds to a vortex filament with an added swirl component. We first show, in the top row of figure 1, how the full 3D and the axisymmetric code find the same minimiser for low values of a , but find different minimisers for high values. Configuration A, at $a = 75.0$, is still in the regime where the global minimiser is rotationally symmetric. At configuration B, for $a = 125.0$, the symmetry-broken branch has already appeared, but is still very close to the symmetric one. Configuration C, at $a = 197.6$, is in a regime where the symmetry broken minimiser clearly dominates the symmetric minimiser. The asymmetric minimising configurations correspond to vortex tubes with a symmetry-breaking helical vortex structure around it that displays only reflection symmetry instead of full axial symmetry. Due to the symmetry of the minimisation problem under reflection with respect to the $z = 0$ plane, the behaviour is identical for negative a , with a mere sign-flip in ω (not shown).

Note that around the point of symmetry breaking, the full 3D code picks up both the symmetric and asymmetric minimisers until the symmetric configuration eventually becomes unstable, as indicated by the two blue dashed lines in the inset of figure 1 (top), where the upper line corresponds to the rotationally symmetric local minimiser of the full 3D code. There is a small difference between the rotationally symmetric minimiser of the full 3D code, and the same minimiser for the axisymmetric code, which is the result of numerical differences in the integration schemes and coordinate systems.

We can compare the instanton configuration against structures observed in DNS, conditioned on observing an extreme vorticity event [1]. The result of this ‘‘filtering’’ procedure [18] is shown in figure 2 (left three columns) for the axisymmetric configuration only. Concretely, this compares an instanton for $\omega_z = a = 60.0$, which would be located left of configuration A in figure 1, in cylindrical coordinates, against the conditional average of DNS data at $\varepsilon = 250$, conditioned on $\omega_z = 60.0$. To compute this average, we integrate 10^4 independent realisations of the 3D NSE (12) on $\Omega = [0, 2\pi]^3$ for a total time of $T = 1$ used in all computations throughout this paper (which is much larger than the large eddy turnover time $T_{LET} \approx 0.1$ for this ε). Exploiting the statistical isotropy and homogeneity of the system in order to increase the sample

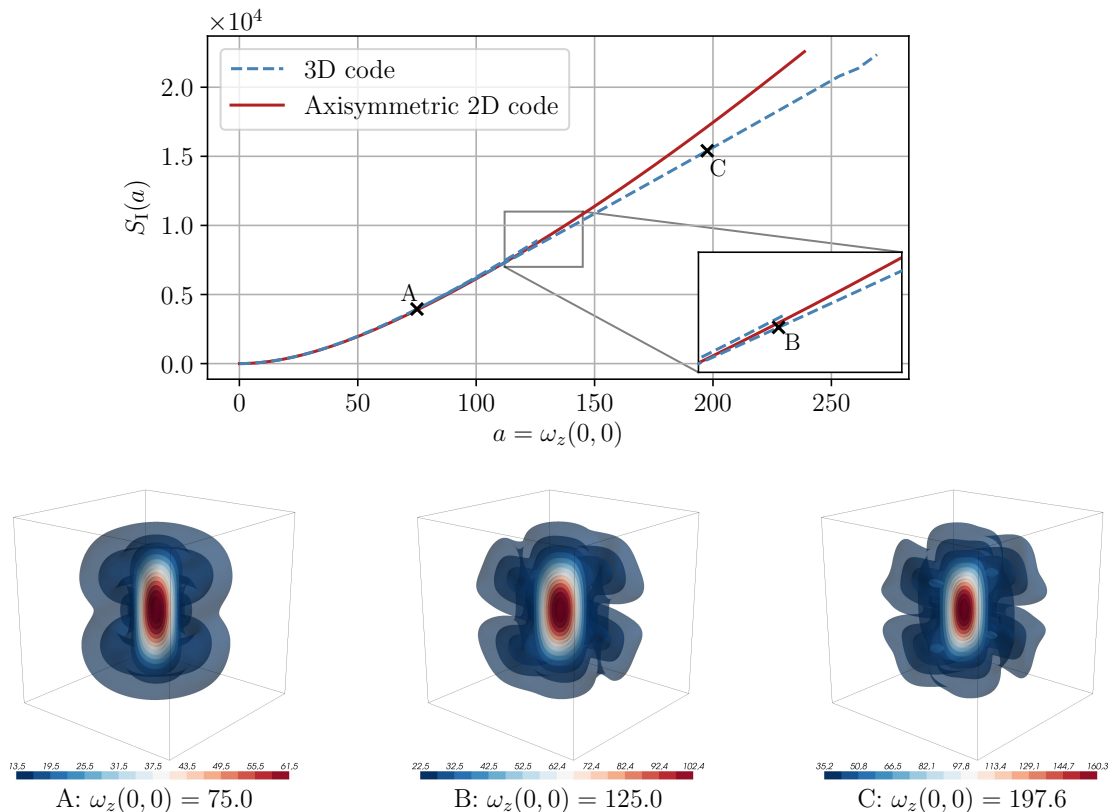


FIG. 1. Results of the full 3D and axisymmetric instanton computations for the vorticity observable $\omega_z(0,0)$. The plot in the top row shows the action $S_I(a)$ at all critical points of the action that were found in our numerical experiments for different values of the final-time constraint $\omega_z(0,0) = a$. The bottom row shows isosurfaces of the vorticity of the final-time configuration of the obtained instanton fields for different observable values as indicated in the top plot. Qualitatively, the field configurations which we observe are vortex tubes in all cases. However, the 3D computations show that a second branch that breaks full rotational symmetry and reduces to reflection symmetry dominates the fully symmetric branch in probability and splits off at $a_c \approx 85$.

size, we analyse the final field configuration for events with $|\|\omega(x)\| - a|/a < 0.01$, and then rotate and translate the coordinate system so that the event is located at $x = (0,0,0)$ and points in z -direction. We average $8.4 \cdot 10^3$ such events, including averaging in θ for each individual event, to obtain the results of figure 2 (top row). The conditional average obtained in this way agrees excellently with the instanton event for the same vorticity, demonstrating that for this Re the most likely and the average configuration realising $\omega_z = 60.0$ are identical, and we are indeed in the large deviation limit.

2. Extreme strain events

Performing the same procedure for the strain observable, $\partial_z u_z(0,0) = a$, we obtain a richer set of outcomes. For the strain, positive and negative observables have different phenomenologies caused by the advection term (see e.g. [38]), but both eventually undergo symmetry breaking. As visible in figure 3 (top), the earliest and most dramatic symmetry breaking is observed for the positive tail of the strain, where an asymmetric branch splits off already at $a_c \approx 14$. Here, the symmetric configuration A, consisting of two counter-rotating, contracting vortex rings, transitions for higher a into an asymmetric sheet/pancake like structure C. We additionally observe a further subdominant symmetry-breaking branch of quadrupole-like configurations B. It is of course difficult to exclude the existence of further subdominant local minimisers, but our numerical experiments where we started the optimisation algorithm either at a random initial condition for the control or at perturbed solutions of previous problems did not show indications of further branches in the considered observable range.

The negative tail has qualitatively similar behaviour at different values a : The symmetric configuration D, corresponding to two colliding vortex rings with opposite orientation, breaks away at $a_c \approx -38$ into more complicated and asymmetric vortex sheet configurations E and F.

The vortex ring structures that we encountered are “trivial” solutions of the instanton equations (14) in cylindrical coordinates in the sense that they satisfy $\omega_r = \omega_\theta \equiv 0$ which does not yield the global minimum of the full action at large observable values. Interestingly, field configurations of this type have previously

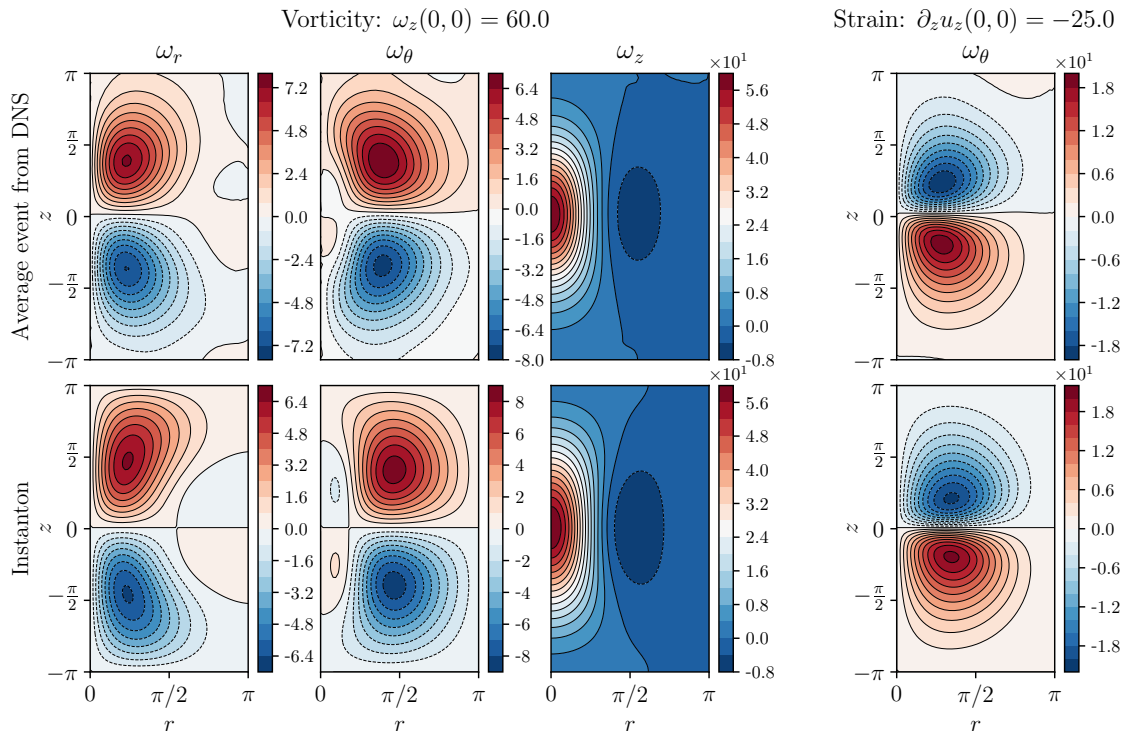


FIG. 2. Comparison of the final-time field configuration of *axisymmetric* vorticity and strain instantons (bottom row) to conditional averages of DNS data for the same prescribed observable values at the origin as the instanton fields (top row). The left three columns show all components of the vorticity in cylindrical coordinates for an event with a prescribed value of $\omega_z(x=0, t=0) = 60.0$ at the origin. The rightmost column only shows the θ component of the vorticity of an event with $\partial_z u_z(x=0, t=0) = -25.0$ since the ω_r and ω_z components are negligibly small. The conditional averages of the DNS data include an angle averaging procedure in θ , and events with suitable observable values at $x \neq 0$ were shifted onto the origin. For the displayed vorticity event, approximately $8.4 \cdot 10^3$ single events as obtained from DNS of (12) with a forcing strength of $\varepsilon = 250$ were averaged, whereas the strain event is an average of approximately $5.1 \cdot 10^3$ events in the same data set.

been found as maximisers of the enstrophy growth rate in [39]. On the other hand, sheet-like structures, as in the symmetry breaking case, have been observed as the most intense dissipative structures already in [40] and in recent spectral simulations using 8192^3 grid points [41].

We further compare the rotationally symmetric strain instanton to the conditional average from DNS in figure 2 (rightmost column). Here, with the data set and procedure as for the vorticity, we only compare the ω_θ -component in cylindrical coordinates, with excellent agreement between the minimiser and the observed conditionally average event realising the strain value of $a = \partial_z u_z(0,0) = -25.0$. For the vortex ring configuration, all other components are negligibly small ($\approx 10^{-4}$ for the 3D instanton code due to numerical noise, $\approx 10^{-1}$ due to statistical noise in the DNS average). We do not compare the symmetry broken instantons to conditional averages, since this would require a much larger data set, where each event, instead of being averaged over θ , is additionally aligned in angular direction, using e.g. the eigenvectors of the velocity gradient tensor.

3. Extreme event probabilities

The derivation of the instanton formalism in section II, and in particular equation (8) make obvious that the instanton not only represents the most likely extreme event, but further allows us to estimate its probability, which scales exponentially with the instanton action. In this section, we compare this prediction for the exponential scaling of the tail with PDFs obtained from DNS, and in particular demonstrate how the symmetry-broken instanton predicts the correct tail scaling for the PDFs, while the axisymmetric instantons dramatically underestimate the likelihood of large strain events. We concentrate on the positive tail of the strain observable in particular, since there the symmetry is broken the earliest and the difference in slope is the clearest.

Figure 4 shows this comparison for three different values $\varepsilon \in \{1, 250, 1000\}$, corresponding to three different Taylor-Reynolds numbers $\text{Re}_\lambda = \sqrt{15\text{Re}} \in \{0.5, 6.4, 10.8\}$ (where Re was determined from the root mean square velocity and integral scale of the data). Note that even the highest Re is still comparably

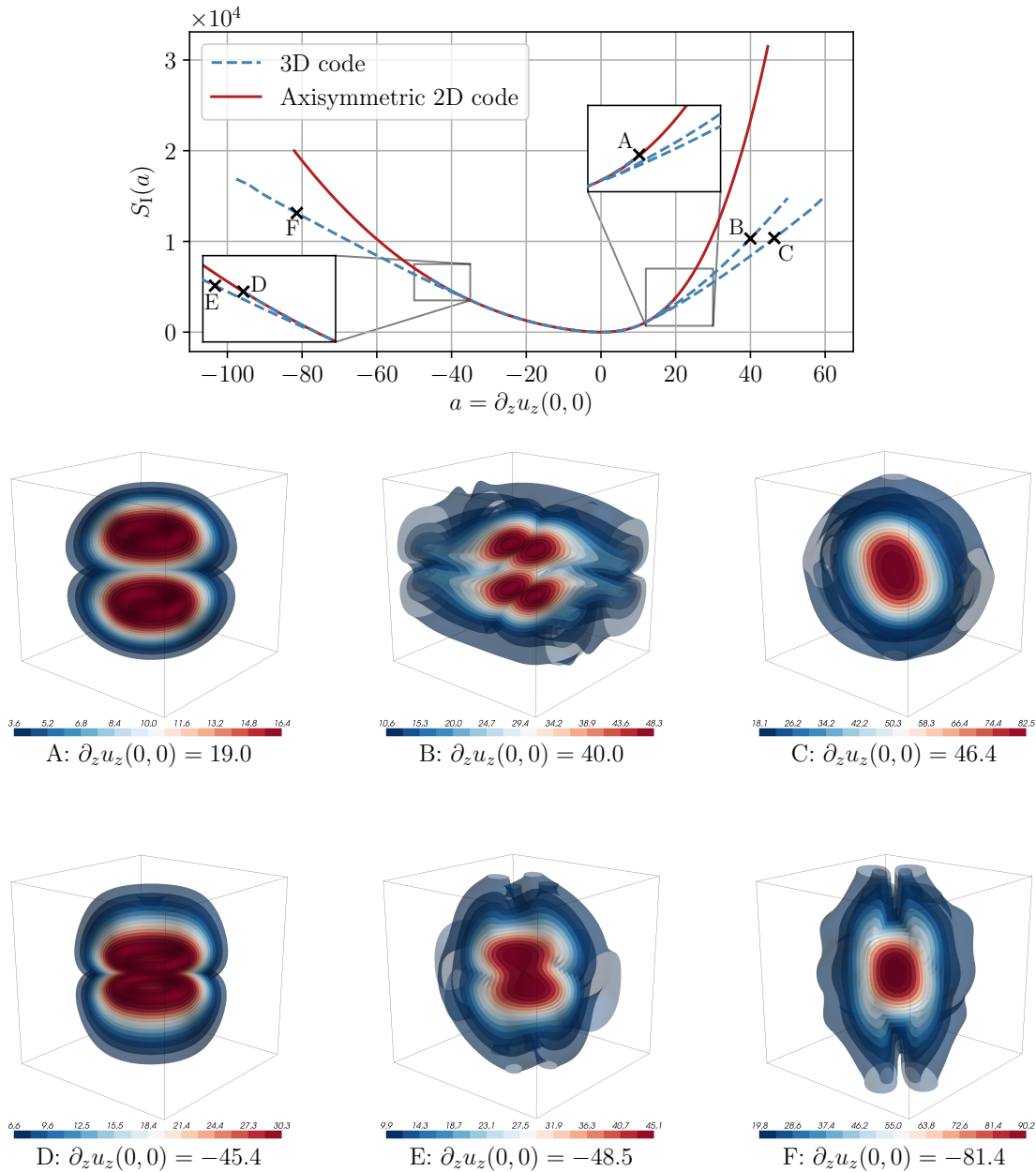


FIG. 3. Results of the axisymmetric and full 3D instanton computations for the strain observable $\partial_z u_z(0,0)$. As in Figure 1, the top plot shows the action at all critical points that were found numerically for different observable values, and the two bottom rows show isosurfaces of the vorticity of the final-time configuration of the indicated instanton fields. Note that, contrary to the vorticity instanton, we find a qualitative difference between the rotationally symmetric strain instanton consisting of two counter-rotating vortex rings (A and D) and a dominant, symmetry-breaking instanton branch that consists of thin vortex sheets (C, E and F). Furthermore, for large positive strain, we find a third, subdominant branch with a quadrupole-like symmetry (B).

low. This is because, as argued in section II 1, for higher Re the instanton is so far in the tail that it cannot be detected in DNS.

For each ε , we performed 10^4 pseudo-spectral simulations of the 3D NSE (12) at a spatial resolution of 128^3 starting from $u_0 = 0$ at $T = -1$ until $t = 0$. The final time configurations were subsampled according to the estimated approximate correlation length $\lambda_{\partial_z u_z} = 0.8$ of the observable, and the shaded area indicates a 95% Wilson score interval [42, 43] for the PDF estimate based on the DNS data. For the lowest Re , the data is almost Gaussian, and the instanton and PDF agree everywhere. No symmetry breaking is observed. For the two higher Re , instead, the instanton approach only captures the tail scaling correctly, since common strain events are not dominated by the instanton in this case. In the tails, though, the axisymmetric instanton clearly underestimates the probability, while the symmetry-broken instanton is in good agreement. This is particularly clear in the right tail of the rightmost panel of figure 4, where the axisymmetric instanton depicted by the red line is far too steep to agree anywhere with the observed tail scaling. This trend continues

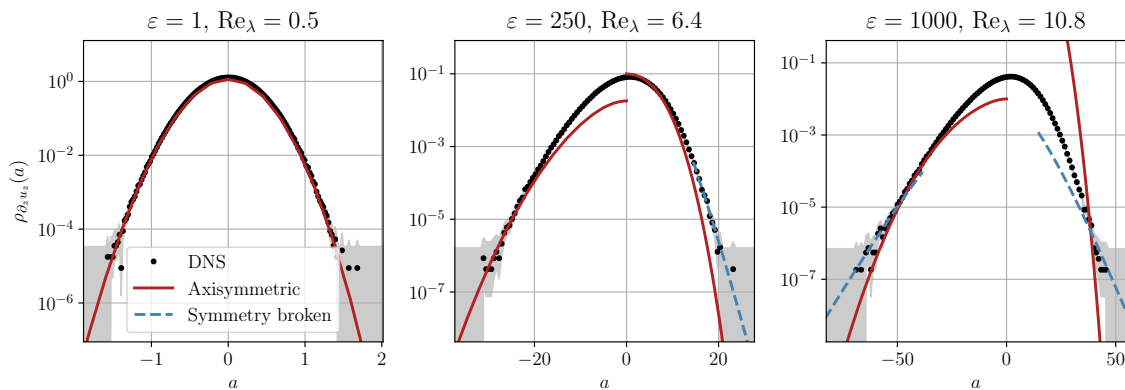


FIG. 4. Comparison of the instanton prediction $\propto \exp\{-\varepsilon^{-1}S_1(a)\}$ for the strain PDF $\rho_{\partial_z u_z}$ to DNS data at different forcing strengths ε or Taylor-Reynolds numbers Re_λ . The dots show the DNS histogram, with a 95% Wilson score interval [42, 43] shaded in grey. The solid lines show the PDF prediction as obtained from the axisymmetric instanton configurations, whereas the dashed lines show the PDF prediction based on the *lowest* symmetry broken branch of the instanton action. Note that we are free to shift all individual branches arbitrarily and independently in the vertical direction in the semi-logarithmic PDF plot since we are only interested in asymptotic scaling estimates. Observe in particular that the axisymmetric strain instanton clearly underestimates the right tail even at the small Reynolds numbers considered here.

in fully developed turbulence at higher Re: The analysis of larger DNS, e.g. in [4], shows that the strain PDF tails can in fact be described by stretched exponentials $\propto \exp\{-c_\pm |a|^{\vartheta_\pm}\}$ with exponents $\vartheta_\pm < 1$, whereas we find that the exponents in both tails derived from the vortex-ring instanton increase monotonically with $|a|$ and saturate above $\vartheta_+ = 2.5$ in the right tail and above $\vartheta_- = 2$ in the left tail. In contrast, while the $S_1(a)$ -curve that we obtained for the symmetry-broken instantons is still convex in the observable range that we were able to consider at the given resolution, the exponents ϑ_\pm are monotonically decreasing in $|a|$ for this branch and decay below 1.5 for both positive and negative strain.

For the vorticity observable of the same DNS dataset at $\varepsilon \in \{1, 250, 1000\}$, we observe the same qualitative results (not shown): At the lowest Re, the instanton again perfectly describes the PDF, whereas the range of validity of the estimate transitions into the tails at higher Re. Here, however, because the symmetry breaking occurs at relatively higher a and leads to a less dramatic difference in scaling, it is hard to draw as clear a conclusion as in the strain case.

IV. CONCLUSION

In this paper, we set out to numerically compute maximum likelihood realisations of extreme vorticity and strain events in the stochastic incompressible 3D NSE. As an alternative and complement to direct sampling approaches, we rephrased the problem into a deterministic variational framework using sample path large deviation theory, which is particularly suited for rare and extreme events. This led us to consider a (3+1)-dimensional optimisation problem with final-time constraints to enforce large observable values, which we were able to solve using tools from PDE-constrained optimisation. For both observables considered here, we observe symmetry breaking of the minimisers: The vortex filaments that lead to large values of the vorticity reduce from axial to reflection symmetry, and the vortex rings that realise large strain transition to a pancake-like vortex sheet structure. For positive strain in particular, we demonstrated that the symmetry-broken minimiser clearly dominates the symmetric one and can in fact be confirmed to yield the correct scaling of DNS PDFs at suitable Re, in contrast to the axisymmetric one.

The possibility to access the most extreme events in Navier-Stokes turbulence without sampling is attractive. Despite the fact that the optimisation problem (9) to be solved is massive, with fields of size 512×128^3 , and a single iteration of the minimisation algorithm corresponding to a forward integration of the NSE, and an equally sized backward propagation, we show that this effort pays off for extreme outlier events: Obtaining these same configurations traditionally necessitates either millions of samples of the stochastic NSE (for lower Re), or the regime is completely inaccessible as the events are entirely too rare and extreme to be observed (for higher Re). While one could try to formulate reduced problems in effective coordinates, for example as in [44], our approach yields the most likely configuration without any *a priori* assumptions about its form or physical mechanisms.

In this paper, we only considered the exponential contribution of the minimiser for the PDF. Improved estimates are possible in principle when taking into account the fluctuations around the instantons, as discussed e.g. in [24]. The computational cost of computing this fluctuation determinant is vastly bigger than the already large problem sizes encountered in the optimisation problem in this work. For this approach, it

is further necessary to integrate out the zero mode associated with the symmetry breaking of the instanton. This correction to the PDF was ignored in this paper.

It would be interesting to determine whether the viscous instanton we discussed here has relevance to inertial range properties of turbulent flow. One possible connection is given by the scaling of velocity gradient moments, which, even in the low Reynolds numbers regime, link dissipative statistics to inertial range properties via so-called fusion rules [45–47]. This possible route towards understanding intermittency is the focus of our future work.

ACKNOWLEDGMENTS

TS would like to thank Sebastian Gallon for useful discussions and help regarding the implementation of the CUDA flow solver and framework. TG acknowledges the support received from the EPSRC projects EP/T011866/1 and EP/V013319/1.

APPENDIX: SUPPLEMENTAL MATERIAL

Appendix A: Introduction and Outline

In this supplemental material, we describe in detail the numerical algorithms that we use to minimise the Freidlin-Wentzell action functional. This way we compute instantons or maximum likelihood trajectories realising extreme values of vorticity and strain, and estimate the dominant contribution of the minimisers to the vorticity and strain probability density functions (PDFs) for the three-dimensional stochastic Navier-Stokes equations (NSE).

Hoping that these notes might be useful for related problems as well, we will discuss the minimisation problem in a slightly more general setting. Nevertheless, we will also specify all necessary details for the specific implementation of the algorithm for the 3D NSE. In these notes, we focus on expanding on section 2 of the main paper. For a general review of the numerics of the instanton method, we refer to [6, 8]. The main source for the optimisation techniques that we use and that we describe in the following is [32].

1. Setup of the problem

We consider a general d -dimensional system of stochastic partial differential equations (SPDEs)

$$\partial_t u(x, t) + N(u(\cdot, t))(x) = \eta(x, t), \quad \langle \eta(x, t) \eta^\top(x', t') \rangle = \varepsilon \chi(x - x') \delta(t - t'), \quad (\text{A1})$$

for a vector field $u : \Omega \times [-T, 0] \rightarrow \mathbb{R}^d$ on the time interval $[-T, 0]$ with $T > 0$ and deterministic initial condition

$$u(x, -T) = u_0(x). \quad (\text{A2})$$

Here, N denotes a deterministic and possibly spatially non-local nonlinearity. The spatial boundary conditions will be assumed to be periodic, such that the domain $\Omega = \mathbb{T}^d = [0, 2\pi]^d / \sim$ is given by a d -torus. The d -dimensional forcing η is assumed to be Gaussian with zero mean, white in time, and stationary with spatial covariance matrix function $\chi : \Omega \rightarrow \mathbb{R}^{d \times d}$, which will typically only act on large scales in the applications considered here. Finally, the noise strength $\varepsilon \in \mathbb{R}$ is assumed to be a small positive number.

The path integral formulation of the PDF ρ_O of a general, \mathbb{R}^d -valued observable $O[u(\cdot, 0)]$ at $a \in \mathbb{R}^d$ takes the form

$$\rho_O(a) = \int Du \delta(u(\cdot, -T) - u_0) \delta(O[u(\cdot, 0)] - a) J[u] \exp \{ -\varepsilon^{-1} S[u] \}, \quad (\text{A3})$$

where S denotes the Freidlin-Wentzell action [7]

$$S[u] = \frac{1}{2} \int_{-T}^0 dt \mathcal{L}(u, \partial_t u) = \frac{1}{2} \int_{-T}^0 dt (\partial_t u + N(u), \chi^{-1} * [\partial_t u + N(u)])_{L^2(\Omega, \mathbb{R}^d)} \geq 0. \quad (\text{A4})$$

Further, J is an additional term that arises from the noise-to-field transformation $\eta \rightarrow u$ and that is independent of ε . The spatial convolution $*$ appears due to the fact that the forcing is assumed to be spatially stationary, such that

$$\int_{\Omega} d^d x' \chi^{-1}(x, x') \eta(x') = \int_{\Omega} d^d x' \chi^{-1}(x - x') \eta(x') = (\chi^{-1} * \eta)(x). \quad (\text{A5})$$

Here, χ^{-1} denotes the inverse operator of χ in the sense that

$$\int_{\Omega} d^d x' \chi^{-1}(x-x') \chi(x'-x'') = \text{Id } \delta^{(d)}(x-x''). \quad (\text{A6})$$

Hence, in Fourier space, χ^{-1} is given by the pointwise inverse matrix of χ . With χ typically acting only on large scales, as well as taking a purely solenoidal forcing in the application that we consider, this implies that χ will be singular. Hence, χ^{-1} will only be defined on a subspace, and we will discuss how to deal with this singular behaviour below. For the definition of the action functional (A4), it is appropriate to set $S[u] = +\infty$ if $\partial_t u + N(u)$ is not in the image of the spatial convolution with χ , which corresponds to trajectories of the system that are not realisable and hence are assigned a probability of 0.

In an appropriate large deviation limit such as the small noise limit $\varepsilon \rightarrow 0$, the path integral (A3) is dominated by the contribution of the minimum action realisation of the velocity field, or instanton, which we denote by u_I , defined as the solution of

$$\begin{cases} \min_u S[u], \\ \text{subject to } u(\cdot, -T) = u_0, \\ O[u(\cdot, 0)] = a. \end{cases} \quad (\text{A7})$$

Solving this constrained minimisation problem (A7) for a range of values for a , evaluating the action $S_I := S[u_I]$ at the minimum, and expanding the path integral around this minimum directly yields the log-asymptotic scaling of the PDF

$$\rho_O(a) \stackrel{\varepsilon \rightarrow 0}{\asymp} \exp\{-\varepsilon^{-1} S_I(a)\}, \quad (\text{A8})$$

the result of which is analysed in the main text for the three-dimensional NSE. Sharper asymptotics in the sense of a prefactor analysis as in [24] are beyond the scope of the current work.

As discussed in the main text, the instanton is not only relevant as the starting point of a saddle-point approximation to the path integral (A3). It is also a meaningful object in itself as it describes the maximum likelihood path realising a given outcome in the following sense: while the probability of each individual trajectory is 0, tubes of radius R in path space that are centred around the instanton will dominate all other tubes of radius R in probability as $R \rightarrow 0$ and $\varepsilon \rightarrow 0$.

2. Reformulation as an optimal control problem

In order to eliminate the inverse correlation function from the target functional (A4) and to reduce the functional to a quadratic form, we introduce the conjugate momentum

$$p := \nabla_{\partial_t u} \mathcal{L} = \chi^{-1} * [\partial_t u + N(u)]. \quad (\text{A9})$$

We treat p as the only independent variable in the resulting minimisation problem

$$\begin{cases} \min_p S[p] = \min_p \frac{1}{2} \int_{-T}^0 dt (p, \chi * p)_{L^2(\Omega, \mathbb{R}^d)}, \\ \text{s.t. } O[u[p](\cdot, 0)] = a. \end{cases} \quad (\text{A10})$$

In the language of optimal control, the field p is the (distributed) control of the system, and the minimisation is carried out over all such p for which the dependent state variable $u = u[p]$, that solves the p -dependent PDE

$$\begin{cases} \partial_t u + N(u) = \chi * p, \\ u(\cdot, -T) = u_0, \end{cases} \quad (\text{A11})$$

satisfies the final time constraint

$$O[u[p](\cdot, 0)] = a. \quad (\text{A12})$$

Note that only $\chi * p$ enters the target functional and the PDE constraint. This significantly reduces the dimensionality of the optimisation problem if the forcing is highly degenerate, as is the case for our application. This will come in very handy in the context of memory reduction techniques, which we will discuss in section C 5 below. Furthermore, we exploit this observation to invert χ numerically: For an arbitrary input field q , we define $\chi^{-1} * q$ by first projecting q onto the image of χ and by then inverting χ on its domain without its kernel.

Appendix B: Conversion to unconstrained problems

There exist various approaches for reducing the constrained optimisation problem (A10) to a single (or a series of) unconstrained optimisation problem(s). We will present a selection in the following. Afterwards, in section C, we will discuss the solution of the resulting unconstrained problems by means of gradient based methods.

1. Method of Lagrange multipliers

The conceptually easiest way to incorporate the final time constraint (A12) into the objective consists in introducing a Lagrange multiplier $\mathcal{F} \in \mathbb{R}^{d'}$. This results in the new objective

$$L[p, \mathcal{F}] = S[p] + (\mathcal{F}, O[u[p](\cdot, 0)] - a)_{d'}. \quad (\text{B1})$$

Essentially, the additional parameter \mathcal{F} has to be tuned in such a way that the final time constraint of u is fulfilled. Note that a minimum of S will always be at a saddle point of L , since the constraint in (B1) is added linearly.

In the context of the one-dimensional stochastic Burgers equation, Chernykh and Stepanov (“CS”, [10]) used the method of Lagrange multipliers to compute instantons for the PDF of the velocity gradient $O[u(\cdot, 0)] = \partial_x u(0, 0)$. They propose to keep \mathcal{F} fixed during the solution of each optimisation problem, instead of adjusting \mathcal{F} iteratively during the computation. The latter would be necessary for the computation of the minimiser for a prescribed value of a that is defined *a priori*. The approach of keeping \mathcal{F} fixed can be interpreted as a specific variant of the method of Lagrange multipliers, when applied to the problem of computing multiple instantons over a range of possible observable values a for the PDF estimate. As a result of inverting the mapping between \mathcal{F} and a , only a single optimisation problem needs to be solved for computing a for a given \mathcal{F} , whereas typically a *series* of unconstrained optimisation problems needs to be solved for fixing a a priori. We will refer to this procedure as the CS approach or CS method, which is summarised in algorithm 1.

This approach works well for computing PDFs over a range of values of a . In that case, one can solve a single unconstrained optimisation problem for each \mathcal{F} in a specified range and simply check *a posteriori* (after the solutions of these unconstrained problems have been found) to which observable value a the computed solution (p_I, u_I) corresponds. If this approach is feasible, it is numerically cheaper than solving a series of unconstrained problems in order to find the minimiser for given values of a . In general, however, there are several problems with this approach, as the map $\mathcal{F} \mapsto a$ can become multivalued or diverge.

In particular, this is relevant whenever the PDF that we want to estimate displays heavy tails in the sense that ρ_O decays slower than $\exp\{-c\|a\|\}$, or more generally if the map $a \mapsto S_I(a)$ fails to be convex, as discussed in [31]; there, nonlinear transformations of the observable that convexify the action are proposed as a solution to this problem.

Regarding the 3D NSE application, we applied the CS approach of varying \mathcal{F} and obtaining a a posteriori only for the axisymmetric instantons. In this case we did not expect either heavy tails or non-unique instantons based on our numerical experiments and therefore made use of the faster solution times compared to the approaches described below.

ALGORITHM 1. CS method for the constrained instanton optimisation problem (A10)

Input:

Fixed Lagrange multiplier $\mathcal{F} \in \mathbb{R}^{d'}$;
 Initial control $p^{(0)}$ (e.g. $p^{(0)} \equiv 0$, or random initialisation, or result from previously solved problem);
 Error tolerance δ .

Output:

Control $p^{(*)}$;
 Action $S[p^{(*)}]$;
 Observable value $a^{(*)}$ for $p^{(*)}$

Starting from $p^{(0)}$, approximately determine a minimum $p^{(*)}$ of $L[p, \mathcal{F}]$ with

$$\left\| \frac{\delta L}{\delta p} [p^{(*)}, \mathcal{F}] \right\|_{L^2(\Omega \times [-T, 0], \mathbb{R}^d)} < \delta,$$

where L is the target functional (B1), and possible algorithms are described in section C.
 Evaluate $S[p^{(*)}]$ and $a^{(*)} = O[u[p^{(*)}](\cdot, 0)]$.

2. Penalty method

As an alternative to the introduction of a Lagrange multiplier for the final time constraint (A12), one can also use a penalty approach: We introduce a penalty parameter $\mu > 0$ and consider the objective

$$R[p, \mu] = S[p] + \frac{\mu}{2} \|O[u[p](\cdot, 0)] - a\|_{d'}^2. \quad (\text{B2})$$

It is intuitively clear and can be proven rigorously that, for $\mu \rightarrow \infty$, minima of R will fulfil the constraint (A12) for the prescribed value of a . For a finite value of μ , there is a trade-off between minimising the quadratic action functional S and minimising the penalty for deviations of $O[u[p](\cdot, 0)]$ from a , which is measured by the second term in (B2). For small values of μ we essentially ignore the additional constraint. We note that the functional (B2) is bounded from below by 0, which is in contrast to the situation in (B1).

Numerically, it is not possible to take the limit $\mu \rightarrow \infty$. Instead, one solves a series of unconstrained optimisation problems with penalty parameters $(\mu^{(m)})_{m=0, \dots, M}$, where $\mu^{(m)}$ increases with m . Using the solution of the previous problem as the initial configuration for the next iteration and verifying the convergence of $O[u[p](\cdot, 0)]$ towards a , approximate solutions to (A10) can be obtained. The choice of step sizes for the penalty parameters $\mu^{(m)}$, as well as the maximum penalty $\mu^{(M)}$ and the termination criterion for the solution of each individual unconstrained optimisation problem need to be considered carefully.

Different to the Lagrange approach, for this approach one cannot (easily) avoid having to solve multiple optimisation problems by taking a short-cut. The penalty method is summarised in algorithm 2.

ALGORITHM 2. Penalty method for the constrained instanton optimisation problem (A10)

Input:

Target observable value $a \in \mathbb{R}^{d'}$;
 Initial control $p^{(0)}$ (e.g. $p^{(0)} \equiv 0$, or random initialisation, or result from previously solved problem);
 Increasing sequence $\mu^{(0)}, \dots, \mu^{(M)}$ of penalty parameters;
 Decreasing sequence $\delta^{(0)}, \dots, \delta^{(M)}$ of error tolerances for each unconstrained minimisation problem.

Output:

Control $p^{(M)}$;
 Action $S[p^{(M)}]$;
 Observable value $a^{(M)}$ for $p^{(M)}$

for $m = 0, 1, 2, \dots, M - 1$ **do**

Starting from $p^{(m)}$, approximately determine a minimum $p^{(*)}$ of $R[p, \mu^{(m)}]$ with

$$\left\| \frac{\delta R}{\delta p} [p^{(*)}, \mu^{(m)}] \right\|_{L^2(\Omega \times [-T, 0], \mathbb{R}^d)} < \delta^{(m)},$$

where R is the quadratic target functional (B2), and minimisation algorithms are described in section C.

Set $p^{(m+1)} \leftarrow p^{(*)}$.

end for

Evaluate $S[p^{(M)}]$ and $a^{(M)} = O[u[p^{(M)}](\cdot, 0)]$.

3. Augmented Lagrangian method

As a third possibility, both of the previous methods can be combined. This results in the so-called augmented Lagrangian method, which is the method that we have applied for the fully three-dimensional NSE instanton computations. In this approach, one introduces both a Lagrange multiplier $\mathcal{F} \in \mathbb{R}^{d'}$ and a penalty parameter $\mu > 0$, which yields the functional

$$L_A[p, \mathcal{F}, \mu] = S[p] + (\mathcal{F}, O[u[p](\cdot, 0)] - a)_{d'} + \frac{\mu}{2} \|O[u[p](\cdot, 0)] - a\|_{d'}^2, \quad (\text{B3})$$

which is again bounded from below. As for the penalty approach, it is necessary to solve a series of optimisation problems for an increasing sequence of penalty parameters $(\mu^{(m)})_{m=0, \dots, M}$ in order to obtain an approximate solution of the constrained problem (A10) with a prescribed value of a . However, it can be shown that, by updating the Lagrange multiplier $\mathcal{F}^{(m)}$ according to

$$\mathcal{F}^{(m+1)} = \mathcal{F}^{(m)} + \mu^{(m)} \left(O[u[p^{(m)}](\cdot, 0)] - a \right), \quad (\text{B4})$$

where $p^{(m)}$ denotes the solution of the m -th unconstrained optimisation problem, the convergence of $O[u[p^{(m)}](\cdot, 0)]$ towards a can be accelerated. As a result, it suffices to consider smaller values of $\mu^{(M)}$ for this method compared to the pure penalty approach. This in turn avoids potential issues with ill-conditioning caused by large penalty parameters. The augmented Lagrangian method is summarised in algorithm 3.

ALGORITHM 3. Augmented Lagrangian method for the constrained instanton optimisation problem (A10)

Input:

Target observable value $a \in \mathbb{R}^{d'}$;
 Initial control $p^{(0)}$ (e.g. $p^{(0)} \equiv 0$, or random initialisation, or result from previously solved problem);
 Initial guess for the Lagrange multiplier $\mathcal{F}^{(0)} \in \mathbb{R}^{d'}$;
 Increasing sequence $\mu^{(0)}, \dots, \mu^{(M)}$ of penalty parameters;
 Decreasing sequence $\delta^{(0)}, \dots, \delta^{(M)}$ of error tolerances for each unconstrained minimisation problem.

Output:

Control $p^{(M)}$;
 Action $S[p^{(M)}]$;
 Observable value $a^{(M)}$ for $p^{(M)}$

for $m = 0, 1, 2, \dots, M - 1$ **do**

Starting from $p^{(m)}$, approximately determine a minimum $p^{(*)}$ of $L_A[p, \mathcal{F}^{(m)}, \mu^{(m)}]$ with

$$\left\| \frac{\delta L_A}{\delta p} [p^{(*)}, \mathcal{F}^{(m)}, \mu^{(m)}] \right\|_{L^2(\Omega \times [-T, 0], \mathbb{R}^d)} < \delta^{(m)}$$

where L_A is the quadratic target functional (B3), and minimisation algorithms are described in section C).

Set $p^{(m+1)} \leftarrow p^{(*)}$.

Set $\mathcal{F}^{(m+1)} \leftarrow \mathcal{F}^{(m)} + \mu^{(m)} \left(O[u[p^{(m)}](\cdot, 0)] - a \right)$.

end for

Evaluate $S[p^{(M)}]$ and $a^{(M)} = O[u[p^{(M)}](\cdot, 0)]$.

Appendix C: Gradient-based minimisation: Gradient descent and L-BFGS method

In the previous section, the solution of the constrained optimisation problem (A10) was reduced to the solution of unconstrained optimisation problems involving different functionals, which can all be considered as special cases of

$$L_A[p, \mathcal{F}, \mu] = \frac{1}{2} \int_{-T}^0 dt (p, \chi * p)_{L^2(\Omega, \mathbb{R}^d)} + (\mathcal{F}, O[u[p](\cdot, 0)] - a)_{d'} + \frac{\mu}{2} \|O[u[p](\cdot, 0)] - a\|_{d'}^2. \quad (\text{C1})$$

We still have the PDE-constraint (A11) but have removed the final time constraint (A12).

In this section, we discuss gradient-based algorithms to minimise this objective numerically with respect to p for fixed parameters $\mu > 0$ and $\mathcal{F} \in \mathbb{R}^{d'}$. We will first derive in section C 1 the first order necessary conditions at minima of (C1), which are typically referred to as instanton equations in this context. In the literature, these instanton equations are often solved iteratively by repeated forward and backward integration. We connect this approach to gradient-based minimisation of (C1) by conveniently expressing the gradient $\delta L_A / \delta p$ using an adjoint state in section C 2. Afterwards, in section C 3, we describe the standard gradient descent algorithm for minimising (C1). In section C 4, we present the L-BFGS scheme. This algorithm has significantly better convergence properties than the standard gradient descent, especially for ill-conditioned problems. Just like gradient descent though, only gradient evaluations are needed and it is not necessary to compute second-order information in form of a Hessian, which is typically very expensive. We conclude by presenting implementational details concerning the memory usage in section C 5.

1. Instanton equations

Here, we derive the instanton equations, i.e. the first order necessary optimality conditions for minima of (C1). In order to easily formulate these conditions, we introduce another, field-valued Lagrange multiplier z , the so called *adjoint variable*. We focus on the case $\mu = 0$, i.e., only consider the method of Lagrange multipliers from section B 1. To formally derive the optimality conditions, we define

$$\begin{aligned} \tilde{L}[u, p, z, \mathcal{F}] = & \frac{1}{2} \int_{-T}^0 dt (p, \chi * p)_{L^2(\Omega, \mathbb{R}^d)} + \int_{-T}^0 dt (z, \partial_t u + N(u) - \chi * p)_{L^2(\Omega, \mathbb{R}^d)} \\ & + (z(\cdot, -T), u(\cdot, -T) - u_0)_{L^2(\Omega, \mathbb{R}^d)} + (\mathcal{F}, O[u(\cdot, 0)] - a)_{d'}. \end{aligned} \quad (\text{C2})$$

The first order necessary conditions then imply the following conditions to hold

$$\begin{cases} \frac{\delta \tilde{L}}{\delta u} = -\partial_t z + \nabla N(u)^\top z = 0, & z(\cdot, 0) = -\left[\frac{\delta O}{\delta u}(u(0))\right]^\top \mathcal{F}, \\ \frac{\delta \tilde{L}}{\delta p} = \chi * [p - z] = 0, \\ \frac{\delta \tilde{L}}{\delta z} = \partial_t u + N(u) - \chi * p = 0, & u(\cdot, -T) = u_0, \\ \nabla_{\mathcal{F}} \tilde{L} = O[u(\cdot, 0)] - a = 0. \end{cases} \quad (\text{C3})$$

Here, the transpose is taken with respect to the scalar product of the space $L^2(\Omega, \mathbb{R}^d)$. Within our definition of χ^{-1} , the second condition implies that for stationary points $(u_1, p_1, z_1, \mathcal{F}_1)$ of the Lagrange function, the equality $p_1 = z_1$ holds. This results in the instanton equations

$$\begin{cases} \partial_t u_1 + N(u_1) = \chi * p_1, & u_1(\cdot, -T) = u_0, \\ \partial_t p_1 - \nabla N(u_1)^\top p_1 = 0, & p_1(0) = -\left[\frac{\delta O}{\delta u}(u_1(0))\right]^\top \mathcal{F}_1. \end{cases} \quad (\text{C4})$$

with \mathcal{F}_1 being chosen such that final time constraint $O[u(\cdot, 0)] - a = 0$ is satisfied.

In [10], CS solved these saddle-point equations numerically by an iterative forward and backward solution of (C4). The connection to gradient-based minimisation methods will be reviewed in the next two sections.

2. Adjoint state method

We continue by explaining how the gradient $\delta L_A / \delta p$ can be computed using the adjoint state method, which involves the solution of a forward and a backward PDE. While this could also be derived from the approach of the previous section (see e.g. [48]), we demonstrate here directly that this is a valid way of expressing the gradient $\delta L_A / \delta p$ at any p , and not only at critical points of L_A . Expanding L_A to first order in δp , we have

$$\begin{aligned} L_A[p + \delta p, \mathcal{F}, \mu] &= L_A[p, \mathcal{F}, \mu] + \int_{-T}^0 dt (\delta p, \chi * p)_{L^2(\Omega, \mathbb{R}^d)} \\ &+ \int_{\Omega} d^d x' \int_{-T}^0 dt \int_{\Omega} d^d x \left(\mathcal{F} + \mu (O[u[p](\cdot, 0)] - a), \frac{\delta O}{\delta u} \Big|_{u(0)}(x') \underbrace{\frac{\delta u(x', 0)}{\delta p(x, t)}}_{=: J(x', t'=0; x, t)} \delta p(x, t) \right)_{d'}. \end{aligned} \quad (\text{C5})$$

We now further simplify the second term. In order to be able to express it in a convenient formulation, we define the adjoint field $z : \Omega \times [-T, 0] \rightarrow \mathbb{R}^d$ as the solution of

$$\begin{cases} \partial_t z - \nabla N(u)^\top z = 0, \\ z(0) = -\left[\frac{\delta O}{\delta u}(u[p](\cdot, 0))\right]^\top \{ \mathcal{F} + \mu (O[u[p](\cdot, 0)] - a) \}. \end{cases} \quad (\text{C6})$$

We now use z to rewrite the inner integral of the second term in (C5) by first computing the expression

$$\begin{aligned} &\partial_{t'} \int_{\Omega} d^d x' (z(x', t'), J(x', t'; x, t) \delta p(x, t))_d \\ &= \int_{\Omega} d^d x' (\partial_{t'} z(x', t'), J(x', t'; x, t) \delta p(x, t))_d + \left(z(x', t'), \left[\frac{\delta}{\delta p(x, t)} \partial_{t'} u(x', t') \right] \delta p(x, t) \right)_d \\ &= \int_{\Omega} d^d x' \left(\nabla N^\top(u(\cdot, t'))(x') z(x', t'), J(x', t'; x, t) \delta p(x, t) \right)_d \\ &\quad + (z(x', t'), [-\nabla N(u(\cdot, t'))(x') J(x', t'; x, t) + \chi(x - x') \delta(t - t')] \delta p(x, t))_d \\ &= ((\chi * z)(x, t'), \delta p(x, t))_d \delta(t - t'). \end{aligned} \quad (\text{C7})$$

Now, integrating (C7) from $t' = -T$ to $t' = 0$, we get (with $J(x', -T; x, t) = 0$)

$$\int_{\Omega} d^d x' (z(x', 0), J(x', 0; x, t) \delta p(x, t))_d = ((\chi * z)(x, t), \delta p(x, t))_d. \quad (\text{C8})$$

Finally, using the final condition in (C6) and combining that with (C5), we arrive at

$$\frac{\delta L_A}{\delta p} = \chi * (p - z). \quad (\text{C9})$$

We observe that for a single evaluation of the gradient of L_A with respect to p , we need to solve two PDEs: First, given the current control p , we need to integrate the nonlinear equations (A11) forward in time in order to determine $u[p]$. Afterwards, we need to integrate the linearised equations (C6) backwards in time from $t = 0$ to $t = -T$. Here, both the starting condition for z at $t = 0$ and the term $\nabla N(u)^\top$ will in general depend on u . We note that due to the negative sign in front of the term $\nabla N(u)^\top z$ in the adjoint equations, integrating these equations backwards in time is actually the natural and numerically stable choice.

3. Minimisation algorithms – Gradient descent

Being able to compute the gradient of the target functional, we can now discuss gradient-based minimisation algorithms. Generally, we consider iterative minimisation algorithms, where the approximation to the optimal control p is updated as

$$p^{(k+1)} = p^{(k)} + \sigma^{(k)} s^{(k)},$$

with $s^{(k)}$ being the search direction and $\sigma^{(k)} \in \mathbb{R}_+ \setminus \{0\}$ being the step length. We first consider the simplest approach for computing the search direction s , which is to choose the direction of steepest descent given by $-\delta L_A / \delta p$. We precondition the search direction s via

$$s = -\chi^{-1} * \frac{\delta L_A}{\delta p} = -(p - z). \quad (\text{C10})$$

To compute the step length σ , we use Armijo line search with backtracking. The full scheme is summarised in algorithm 4 and will be discussed in more detail in the following.

The preconditioner used in (C10), i.e. the correlation matrix, corresponds to the Hessian or second variation of the functional L_A in the linear case (i.e., when both N and O are linear and $\mu = 0$). It significantly improves the convergence of the scheme in numerical experiments with rapidly decaying χ . Indeed, with this preconditioner, the update steps for $p^{(k)}$ read

$$p^{(k+1)} = p^{(k)} + \sigma^{(k)} s^{(k)} = (1 - \sigma^{(k)}) p^{(k)} + \sigma^{(k)} z^{(k)}, \quad (\text{C11})$$

which is precisely the weighted update scheme of [10] for an iterative solution of (C4), which has been presented as a fixed-point like iteration there.

Different to [10], we compute the step length using Armijo line search with backtracking. It can be shown that gradient descent with Armijo line search converges to stationary points of minimisation problems under suitable conditions. For our specific case, the *Armijo* condition, also called *sufficient decrease* condition, is given by

$$L_A [p^{(k+1)}, \mathcal{F}, \mu] \leq L_A [p^{(k)}, \mathcal{F}, \mu] + c \sigma^{(k)} \left(g^{(k)}, s^{(k)} \right)_{L^2(\Omega \times [-T, 0], \mathbb{R}^d)}, \quad (\text{C12})$$

where $g^{(k)}$ is the gradient at $p^{(k)}$ and $c > 0$ is the sufficient decrease constant. Using the definition (C1) of the target functional, this condition can be rewritten as

$$\begin{aligned} & \sigma^{(k)} \left(p^{(k)}, \chi * s^{(k)} \right)_{L^2(\Omega \times [-T, 0], \mathbb{R}^d)} + \frac{(\sigma^{(k)})^2}{2} \left(s^{(k)}, \chi * s^{(k)} \right)_{L^2(\Omega \times [-T, 0], \mathbb{R}^d)} \\ & \leq \left(\mathcal{F}, O[u[p^{(k)}](\cdot, 0)] - O[u[p^{(k+1)}](\cdot, 0)] \right)_{d'} + \frac{\mu}{2} \left\{ \left\| O[u[p^{(k)}](\cdot, 0)] - a \right\|_{d'}^2 \right. \\ & \quad \left. - \left\| O[u[p^{(k+1)}](\cdot, 0)] - a \right\|_{d'}^2 \right\} + c \sigma^{(k)} \left(g^{(k)}, s^{(k)} \right)_{L^2(\Omega \times [-T, 0], \mathbb{R}^d)}. \end{aligned} \quad (\text{C13})$$

We note that all L^2 scalar products in this inequality only need to be evaluated once for each complete line search as they stay the same for different values of $\sigma^{(k)}$. Due to the appearance of $O[u[p^{(k+1)}](\cdot, 0)]$, however, it is necessary to integrate (A11) once for each step size $\sigma^{(k)}$ that is considered in the line search loop.

The approach that we described above and that we applied for minimising (C1) is called *optimise then discretise*: we first set up the optimality system (on a continuous level) and then discretise each equation. The alternative approach is called *discretise then optimise*. Here, one first discretises the optimal control problem, in particular the state equation, and then derives optimality conditions for the discretised problem, which can be a very tedious thing to do. Ideally, both approaches commute. If this is not the case, one could end up with inconsistent gradient discretisations for the approach of *optimise then discretise*, which potentially result in the break down of the gradient scheme. Typically, increasing the resolution in this case

results in better gradient approximations and therefore cures (part of) the problem. It is generally better though to address the problem by choosing the discretisation of the state and the adjoint equations very carefully, ideally in such a way to ensure commutativity of the approaches.

For the kind of problems considered here, one needs to make sure that the time stepping schemes for the forward and backward equations and the quadrature rules for the time integral that appears in the L^2 integrals are a good fit to each other. As an additional safeguard for inconsistencies in the gradient computation, we implemented a break condition for the case that the step size considered by the line search algorithm becomes too small. If the algorithm stops early due to this criterion, then one has to check individually whether the current accuracy is enough for the application at hand, or if an increased resolution is necessary, which often leads to a better gradient approximation. In our case, it helped to increase the resolution of the time stepping scheme.

Finally, we remark that the most natural stopping criterion for the gradient descent algorithm is to require that $\|g^{(k)}\|_{L^2(\Omega \times [-T, 0], \mathbb{R}^d)}$ is smaller than a given threshold tolerance. We therefore use this stopping criterion instead of checking whether the relative changes of the observable $a^{(k)}$ from one step to the next are below a threshold, as suggested in [6].

ALGORITHM 4. Gradient descent for the minimisation of (C1)

Input:

Target observable value $a \in \mathbb{R}^d$;
 Penalty parameter $\mu > 0$;
 Lagrange multiplier $\mathcal{F} \in \mathbb{R}^d$;
 Initial control $p^{(0)}$ (e.g. $p^{(0)} \equiv 0$, or random initialisation, or result from previously solved problem);
 Error tolerance δ ;
 Maximum step number K ;
 Initial step size $\sigma_{\text{init}} > 0$ (typically $\sigma_{\text{init}} = 1$);
 Minimum step size $\sigma_{\text{min}} \ll \sigma_{\text{init}}$;
 Backtracking fraction $\beta \in (0, 1)$ (e.g. $\beta = 1/2$);
 Sufficient decrease constant $c > 0$ (typically $c \approx 10^{-2}$).

Output:

Control $p^{(*)}$ (approximate minimum of L_A);
 Gradient norm $\|\delta L_A / \delta p(p^{(*)})\|_{L^2(\Omega \times [-T, 0], \mathbb{R}^d)}$ at the approximate minimum;
 Augmented Lagrangian $L_A[p^{(*)}, \mathcal{F}, \mu]$;
 Observable value $a^{(*)}$ for $p^{(*)}$

for $k = 0, 1, 2, \dots, K - 1$ **do**

 Compute the gradient at $p^{(k)}$;
 Starting from u_0 , integrate the forward equation (A11) with $p^{(k)}$ as RHS and store the solution $u^{(k)}$.
 Store the current observable value $a^{(k)} = O[u[p^{(k)}]](\cdot, 0)$.
 Integrate (C6) backwards to get $z^{(k)}$, and compute the gradient

$$g^{(k)} \leftarrow \chi * (p^{(k)} - z^{(k)}).$$

 Compute and store $\|g^{(k)}\|_{L^2(\Omega \times [-T, 0], \mathbb{R}^d)}$.

if $\|g^{(k)}\|_{L^2(\Omega \times [-T, 0], \mathbb{R}^d)} < \delta$ **then**

break

end if

 Fix the search direction

$$s^{(k)} \leftarrow -\chi^{-1} * g^{(k)}$$

 and perform an Armijo line search to determine the step length $\sigma^{(k)}$:

for $\sigma^{(k)} = \sigma_{\text{init}}, \beta \sigma_{\text{init}}, \beta^2 \sigma_{\text{init}}, \dots$ **do**

 Set $p^{(k+1)} \leftarrow p^{(k)} + \sigma^{(k)} s^{(k)}$.

 Evaluate $L_A[p^{(k+1)}, \mathcal{F}, \mu]$ (needs another forward integration).

if $L_A[p^{(k+1)}, \mathcal{F}, \mu] \leq L_A[p^{(k)}, \mathcal{F}, \mu] + c \sigma^{(k)} (g^{(k)}, s^{(k)})_{L^2(\Omega \times [-T, 0], \mathbb{R}^d)}$ **then**

break current loop.

end if

if $\sigma^{(k)} < \sigma_{\text{min}}$ **then**

break current and outer loop; report.

end if

end for

end for

4. Minimisation algorithms – L-BFGS method

While the gradient descent scheme is simple to realise, globally convergent, and robust, its convergence can be very slow if the problem is ill-conditioned. Using the true Hessian of L_A as a preconditioner would result in a significant increase in convergence speed. This would correspond to using an exact Newton scheme, which comes with quadratic convergence instead of the linear convergence that the gradient descent scheme offers (with convergence rates that might be very close to 1 for ill-conditioned problems). Practically, however, it is infeasible to explicitly compute and store all the entries of the discrete Hessian of L_A for the (3+1)-dimensional PDE-constrained optimisation problem in case of the 3D NSE. If we stick to solvers that only require matrix-vector products instead of knowledge of the full matrix, this might be an approach to examine as evaluating the Hessian or its inverse in certain directions is achievable. We plan to do so in future work.

For now, we use *Quasi Newton* schemes. These schemes typically show superlinear convergence. Therefore, they converge significantly faster than the pure gradient scheme. Different to Newton-like approaches, it is not necessary to supply second-order information. Instead, the scheme itself extracts curvature information out of the past steps. A very well-known Quasi Newton method is the so called BFGS scheme. Given that we have to deal with a very high-dimensional optimisation problem here, we use a variant with limited memory requirements, the so called L-BFGS scheme.

For this scheme, one has to store the last m control updates (with m typically being chosen between 3 and 20)

$$\Delta p^{(k-1)} := p^{(k)} - p^{(k-1)}, \dots, \Delta p^{(k-m)} := p^{(k-m+1)} - p^{(k-m)} \quad (\text{C14})$$

as well as the last m gradient updates

$$\Delta g^{(k-1)} := g^{(k)} - g^{(k-1)}, \dots, \Delta g^{(k-m)} := g^{(k-m+1)} - g^{(k-m)}. \quad (\text{C15})$$

From this information, a low-rank approximation of the inverse of the Hessian $H^{(k)} = \delta^2 L_A[p^{(k)}, \mathcal{F}, \mu]$ is computed. This approximation is directly applied to the gradient descent direction $-g^{(k)}$ as a preconditioner, without storing it explicitly. We also note that as a result there is no need to solve linear systems when applying the preconditioner as the algorithm directly computes an approximation to the *inverse* Hessian.

The L-BFGS algorithm is derived as a variant of the standard BFGS scheme, which we will briefly sketch in the following. For the computation of the approximate inverse Hessian, we start with an initial symmetric and positive definite estimate $B^{(0)}$ for the inverse Hessian $H^{(0)}$ at the initial position. Standard choices are $B^{(0)} = \text{Id}$ or a scaled version of that. We use $B^{(0)} = \chi^{-1}$. The standard BFGS scheme for approximating the inverse $B^{(k+1)}$, which is then used to compute the search direction $s^{(k+1)} = -B^{(k+1)}g^{(k+1)}$ at the $(k+1)$ -th step of our iterative method, is given by

$$\begin{aligned} B^{(k+1)} &= B^{(k)} + \rho^{(k)} \left[w^{(k)} \otimes \Delta p^{(k)} + \Delta p^{(k)} \otimes w^{(k)} \right] \\ &\quad - \left[\rho^{(k)} \right]^2 \left(w^{(k)}, \Delta g^{(k)} \right)_{L^2(\Omega \times [-T, 0], \mathbb{R}^d)} \Delta p^{(k)} \otimes \Delta p^{(k)} \\ &= \left[V^{(k)} \right]^\top B^{(k)} V^{(k)} + \rho^{(k)} \Delta p^{(k)} \otimes \Delta p^{(k)}, \end{aligned} \quad (\text{C16})$$

with

$$\rho^{(k)} = \left[\left(\Delta g^{(k)}, \Delta p^{(k)} \right)_{L^2(\Omega \times [-T, 0], \mathbb{R}^d)} \right]^{-1} \quad (\text{C17})$$

as well as

$$w^{(k)} = \Delta p^{(k)} - B^{(k)} \Delta g^{(k)} \quad (\text{C18})$$

and

$$V^{(k)} = \text{Id} - \rho^{(k)} \Delta g^{(k)} \otimes \Delta p^{(k)}. \quad (\text{C19})$$

Theoretical results typically assume that Powell-Wolfe line search is used, which is a fairly expensive algorithm for computing the step length. This guarantees that the matrices $B^{(k)}$ remains positive definite at all steps. In practice, the much cheaper Armijo line search typically works very well. As one no longer has a guarantee about the positive definiteness of $B^{(k)}$, it is recommended to implement safety checks to ensure that $s^{(k+1)}$ is indeed a descent direction, such as the angle condition given by

$$\left(-g^{(k)}, s^{(k)} \right)_{L^2(\Omega \times [-T, 0], \mathbb{R}^d)} \geq \tilde{c} \left\| g^{(k)} \right\|_{L^2(\Omega \times [-T, 0], \mathbb{R}^d)} \left\| s^{(k)} \right\|_{L^2(\Omega \times [-T, 0], \mathbb{R}^d)}, \quad (\text{C20})$$

with a small constant \tilde{c} . This condition guarantees that the angle between the search direction $s^{(k)}$ and the negative gradient $-g^{(k)}$ is smaller than 90 degrees. If the angle condition is violated, a possible remedy would be to reset $B^{(k)}$ to the initial estimate $B^{(0)}$, i.e. to completely reset the BFGS memory.

Using the above formula for $B^{(k+1)}$ for large-scale problems is not recommended as the approximation matrix is usually dense. We therefore rewrite the algorithm to deduce a limited memory version. From the last line of (C16), we see that the BFGS preconditioner can be written recursively as

$$\begin{aligned} B^{(k+1)} &= \left[V^{(k)} \right]^\top B^{(k)} V^{(k)} + \rho^{(k)} \Delta p^{(k)} \otimes \Delta p^{(k)} \\ &= \left[V^{(k-1)} V^{(k)} \right]^\top B^{(k-1)} \left[V^{(k-1)} V^{(k)} \right] \\ &\quad + \rho^{(k-1)} \left[V^{(k)} \right]^\top \Delta p^{(k-1)} \otimes \Delta p^{(k-1)} V^{(k)} + \rho^{(k)} \Delta p^{(k)} \otimes \Delta p^{(k)} \end{aligned} \quad (\text{C21})$$

$$\begin{aligned} &= \dots = \\ &= \left[V^{(k-m+1)} \dots V^{(k)} \right]^\top B^{(k-m+1)} \left[V^{(k-m+1)} \dots V^{(k)} \right] \\ &\quad + \rho^{(k-m+1)} \left[V^{(k-m+2)} \dots V^{(k)} \right]^\top \Delta p^{(k-m+1)} \otimes \Delta p^{(k-m+1)} \left[V^{(k-m+2)} \dots V^{(k)} \right] \\ &\quad + \rho^{(k-m+2)} \left[V^{(k-m+3)} \dots V^{(k)} \right]^\top \Delta p^{(k-m+2)} \otimes \Delta p^{(k-m+2)} \left[V^{(k-m+3)} \dots V^{(k)} \right] \\ &\quad + \dots + \rho^{(k)} \Delta p^{(k)} \otimes \Delta p^{(k)}. \end{aligned} \quad (\text{C22})$$

That means, we can write $B^{(k+1)}$ using the matrix $B^{(k-m+1)}$ and vector products that involve $\Delta p^{(k)}, \dots, \Delta p^{(k-m+1)}$ as well as $\Delta g^{(k)}, \dots, \Delta g^{(k-m+1)}$.

For the L-BFGS scheme one now replaces the potentially dense matrix $B^{(k-m+1)}$ by an initial sparse guess $B_0^{(k+1)}$, which can vary from iteration to iteration. Note that it is not necessary to store full matrices. Only the last m entries for Δp and Δg need to be stored in order to construct the preconditioner. A popular choice for the initial guess would be

$$B_0^{(k+1)} = \gamma^{(k)} \text{Id} = \frac{(\Delta p^{(k)}, \Delta g^{(k)})_{L^2(\Omega \times [-T, 0], \mathbb{R}^d)}}{(\Delta g^{(k)}, \Delta g^{(k)})_{L^2(\Omega \times [-T, 0], \mathbb{R}^d)}} \text{Id}. \quad (\text{C23})$$

Based on numerical experiments for the 1D viscous Burgers equation, we choose

$$B_0^{(k+1)} = \gamma^{(k)} \chi^{-1} \quad (\text{C24})$$

for the problem at hand. The linear operator $B^{(k+1)}$ can be applied to the negative gradient $-g^{(k+1)}$ to compute the search direction $s^{(k+1)}$ without explicitly storing it via the two-loop recursion that is summarised in algorithm 5. The algorithm for the full L-BFGS method is shown in algorithm 6.

Formally, we lose the superlinear convergence property by using this limited memory version. Practically, we still observe dramatic speed-up compared to using a plain gradient descent. Compared to the standard BFGS scheme, we observe a reduction of memory requirements and operations counts by using the L-BFGS scheme.

5. Memory reduction techniques

Here, we briefly comment on memory reduction techniques that allow us to fit a complete optimisation problem of the kind described above in 3 spatial dimensions and 1 time dimension onto a single modern GPU without having to resort to domain decomposition. These points have been previously discussed and quantitatively analysed in detail in [37]. Therefore, we only provide a few remarks in the following about how to extend the ideas presented there to the slightly different setting that we use here.

First, as indicated in section A 2, for highly singular forcing correlation functions χ , the effective dimensionality of the control is rather small: Assuming that χ only acts on large scales, its Fourier transform $\hat{\chi}(k)$ will only be non-zero for a small and *resolution-independent* number of modes $n_{k,\text{eff}}$. In practice, one may either specifically choose a covariance that is strictly set to 0 for all but a finite number of modes, or truncate a given χ at modes where a suitable matrix norm of $\hat{\chi}(k)$ drops below a threshold. The crucial observation is then that in the right-hand side of the state equation (A11), which is given by $\tilde{\chi} * p(k) = \hat{\chi}(k) \hat{p}(k)$, and in the action function

$$S[p] = \frac{1}{2} \int_{-T}^0 dt (p, \chi * p)_{L^2(\Omega, \mathbb{R}^d)} = \frac{1}{2} \int_{-T}^0 dt (2\pi)^d \sum_{k \in \mathbb{Z}^d} (\hat{p}(k), \hat{\chi}(k) \hat{p}(k))_d, \quad (\text{C25})$$

ALGORITHM 5. Two-loop recursion for the evaluation of $s^{(k)} = -B^{(k)}g^{(k)}$

Input:

Current gradient $g^{(k)}$;
 m previous gradient updates $\Delta g^{(k-1)}, \dots, \Delta g^{(k-m)}$;
 m previous control updates $\Delta p^{(k-1)}, \dots, \Delta p^{(k-m)}$;
 m previous weights $\rho^{(k-1)}, \dots, \rho^{(k-m)}$.

Output:

$s^{(k)} = -B^{(k)}g^{(k)}$ given by (C22).

```

 $r \leftarrow -s^{(k)}$ .
for  $i = k-1, \dots, k-m$  do
   $\alpha^{(i)} \leftarrow \rho^{(i)} \left( \Delta p^{(i)}, r \right)_{L^2(\Omega \times [-T, 0], \mathbb{R}^d)}$ .
   $r \leftarrow r - \alpha^{(i)} \Delta g^{(i)}$ .
end for
 $r \leftarrow B_0^{(k)} r$ 
for  $i = k-m, \dots, k-1$  do
   $h \leftarrow \rho^{(i)} \left( \Delta g^{(i)}, r \right)_{L^2(\Omega \times [-T, 0], \mathbb{R}^d)}$ .
   $r \leftarrow r + \left[ \alpha^{(i)} - h \right] \Delta p^{(i)}$ .
end for
return  $r$ .

```

ALGORITHM 6. L-BFGS method for the minimisation of (C1)

Input:

Target observable value $a \in \mathbb{R}^{d'}$;
Penalty parameter $\mu > 0$;
Lagrange multiplier $\mathcal{F} \in \mathbb{R}^{d'}$;
Initial control $p^{(0)}$ (e.g. $p^{(0)} \equiv 0$, or random initialisation, or result from previously solved problem);
Error tolerance δ ;
Maximum step number K ;
Initial step size $\sigma_{\text{init}} > 0$ (typically $\sigma_{\text{init}} = 1$);
Minimum step size $\sigma_{\text{min}} \ll \sigma_{\text{init}}$;
Backtracking fraction $\beta \in (0, 1)$ (e.g. $\beta = 1/2$);
Sufficient decrease constant $c > 0$ (typically $c \approx 10^{-2}$);
Number of stored previous updates m (typically 3 to 20);
Angle condition constant \tilde{c} (typically $\tilde{c} \approx 10^{-4}$).

Output:

Control $p^{(*)}$ (approximate minimum of L_A);
Gradient norm $\|\delta L_A / \delta p(p^{(*)})\|_{L^2(\Omega \times [-T, 0], \mathbb{R}^d)}$ at the approximate minimum;
Augmented Lagrangian $L_A[p^{(*)}, \mathcal{F}, \mu]$;
Observable value $a^{(*)}$ for $p^{(*)}$

```

for  $k = 0, 1, 2, \dots, K-1$  do
  Compute the gradient  $g^{(k)}$  at  $p^{(k)}$  as in algorithm 4.
  if  $k \geq m+1$  then
    Delete  $\Delta g^{(k-m-1)}, \Delta p^{(k-m-1)}$  and  $\rho^{(k-m-1)}$ 
  end if
  if  $k \geq 1$  then
    Store  $\Delta p^{(k-1)}, \Delta g^{(k-1)}$  and  $\rho^{(k-1)} \leftarrow 1 / \left( \Delta g^{(k-1)}, \Delta p^{(k-1)} \right)_{L^2(\Omega \times [-T, 0], \mathbb{R}^d)}$ .
  end if
  Compute and store  $\|g^{(k)}\|_{L^2(\Omega \times [-T, 0], \mathbb{R}^d)}$ .
  if  $\|g^{(k)}\|_{L^2(\Omega \times [-T, 0], \mathbb{R}^d)} < \delta$  then
    break
  end if
  Fix the search direction with algorithm 5:  $s^{(k)} \leftarrow \text{Two-loop} \left( -g^{(k)}, \Delta g, \Delta p, \rho \right)$ , and (C24) as initial guess for  $B_0^{(k)}$ 
  (use  $s^{(k)} \leftarrow -\chi^{-1} * g^{(k)}$  for  $k = 0$ ).
  if (C20) is violated then
    Reset to  $s^{(k)} \leftarrow -\chi^{-1} * g^{(k)}$  and delete all  $\Delta g, \Delta p, \rho$ .
  end if
  Perform an Armijo line search for  $s^{(k)}$  to determine the step length  $\sigma^{(k)}$  as in algorithm 4, and update  $p^{(k+1)} \leftarrow p^{(k)} + \sigma^{(k)} s^{(k)}$ .
end for

```

where we used Parseval's identity, only these $n_{k,\text{eff}}$ modes enter into the problem. Consequently, it is only necessary to store this reduced number of modes. Note in particular that this approach is still valid for the gradient computation and L-BFGS updates. Therefore, it suffices to store the reduced mode representation for the gradient $g^{(k)}$ in each time step, as well as for the previous updates $\Delta p^{(k)}$ and $\Delta g^{(k)}$.

Even though the control only acts on a small number of Fourier modes, the velocity field u and the adjoint field z will still be nonzero at all appearing, small-scale modes, because the state equation is nonlinear in general, and the final condition of the linear adjoint equation may also involve small scales. Hence, even though only the large-scale $n_{k,\text{eff}}$ modes of the gradient are actually used for the updates in the optimisation algorithms, it is necessary to integrate the forward and backward equations (A11) and (C6) on the full grid for each gradient computation. This causes the main costs of the algorithm and is responsible for the scheme being expensive despite the discrete effective control space that we optimise over being comparatively low-dimensional.

Further, in order to be able to integrate the adjoint equation (C6), the full space-time history of $u[p^{(k)}]$ is needed. We avoid having to store this by using a checkpoint strategy for u . We only store instances $u(\cdot, t_k)$ on a logarithmically spaced subgrid in time during the forward integration. The price to pay is to do some redundant computations to compute the information in between, which has not been stored, when it is needed for solving the adjoint equation. Using this logarithmic scaling results in a good balance between saving memory and unnecessary recomputations.

Finally, we remark that the low dimension of the control space suggests that a suitably modified implementation of Newton's method for the minimisation of (C1) could be comparatively cheap. In particular, the determinant of the reduced Hessian of the action functional at the minimiser could be computed in this manner, which would be relevant for numerically computing prefactor estimates to improve (A8). Extensions of the presented algorithms in this direction are left as future work for now (also see the related work [14]).

Appendix D: Three-dimensional Navier-Stokes instanton implementation

The SPDE with which we are concerned in the main text are the 3D NSE in nondimensionalised units

$$\begin{cases} \partial_t u + (u \cdot \nabla)u = -\nabla P + \Delta u + \sqrt{\varepsilon} \eta, \\ \nabla \cdot u = 0, \\ u(\cdot, -T) = u_0, \end{cases} \quad (\text{D1})$$

on $\Omega \times [-T, 0]$ with $\Omega = [0, 2\pi]^3$ with periodic boundary conditions, a strictly solenoidal forcing with $\nabla \cdot \eta = 0$ for each realisation, and initial condition $u_0 = 0$.

1. Derivation of the adjoint equation

In order to directly apply the formalism that has been developed in the previous sections to this example, it is necessary to remove the additional incompressibility constraint $\nabla \cdot u = 0$ from the system. In this section, we will show how this can be done by working with compressible fields as a technical detour. The final optimisation algorithms will, however, be formulated only in terms of incompressible control, state and adjoint variables.

In the incompressible NSE, the constraint $\nabla \cdot u = 0$ on the velocity field is of course enforced through the pressure P , which can be eliminated by taking the divergence of the evolution equation for u and solving for P , leading to

$$P = -\Delta^{-1} \nabla \cdot ((u \cdot \nabla)u). \quad (\text{D2})$$

Using the Leray projection \mathbb{P} onto the divergence-free part of a vector field (see e.g. [26]), which can be written as

$$\mathbb{P} = \text{Id} - \nabla \Delta^{-1} \nabla \cdot, \quad (\text{D3})$$

or

$$\mathbb{P} = \text{Id} - \frac{kk^\top}{\|k\|^2} \quad (\text{D4})$$

in Fourier space, the incompressible NSE can be reduced to

$$\begin{cases} \partial_t u + \mathbb{P}[(u \cdot \nabla)u] = \Delta u + \sqrt{\varepsilon} \eta, \\ u(\cdot, -T) = u_0. \end{cases} \quad (\text{D5})$$

Here, for an initial condition that is divergence-free, the evolution equation then obviously preserves solenoidality. Taking this approach one step further, we may also consider the SPDE

$$\begin{cases} \partial_t v + (\mathbb{P}[v] \cdot \nabla) \mathbb{P}[v] = \Delta v + \sqrt{\varepsilon} \eta, \\ v(\cdot, -T) = v_0 \end{cases} \quad (\text{D6})$$

for a compressible field v without any restrictions on its divergence. In this formulation, the projected field $u := \mathbb{P}[v]$ will solve the incompressible NSE with initial condition $u_0 = \mathbb{P}[v_0]$. The advantage of (D6) is that it is straightforward to compute the transposed differential of the drift term that is needed for the evolution equation for z in the adjoint state method. Similarly, in the field-theoretic formulation that has been briefly discussed in section A 1, it is not necessary to restrict the integration in path space to solenoidal vector fields through the introduction of a functional Lagrange multiplier in this formulation. Now, with

$$N(v) = (\mathbb{P}[v] \cdot \nabla) \mathbb{P}[v] - \Delta v, \quad (\text{D7})$$

and using the fact that \mathbb{P} is self-adjoint with respect to the $L^2(\Omega, \mathbb{R}^3)$ scalar product for periodic vector fields, we obtain

$$\begin{aligned} \left(\nabla N(v)^\top w, \delta v \right)_{L^2(\Omega, \mathbb{R}^3)} &= \left(w, \frac{d}{dh} \Big|_{h=0} N(v + h\delta v) \right)_{L^2(\Omega, \mathbb{R}^3)} \\ &= (w, (\mathbb{P}[\delta v] \cdot \nabla) \mathbb{P}[v] + (\mathbb{P}[v] \cdot \nabla) \mathbb{P}[\delta v] - \Delta \delta v)_{L^2(\Omega, \mathbb{R}^3)} \\ &= \int_{\Omega} d^3x w_i (\mathbb{P}[\delta v]_j \partial_j \mathbb{P}[v]_i + \mathbb{P}[v]_j \partial_j \mathbb{P}[\delta v]_i - \partial_j \partial_j \delta v_i) \\ &= \int_{\Omega} d^3x [-\mathbb{P}[v]_i \partial_j w_i \mathbb{P}[\delta v]_j - \mathbb{P}[v]_j \partial_j w_i \mathbb{P}[\delta v]_i - \delta v_i \partial_j \partial_j w_i] \\ &= \left(-\mathbb{P} \left[(\mathbb{P}[v] \cdot \nabla) w + (\nabla w)^\top \mathbb{P}[v] \right] - \Delta w, \delta v \right)_{L^2(\Omega, \mathbb{R}^3)}. \end{aligned} \quad (\text{D8})$$

Despite this excursion using compressible vector fields, the instanton equations (C4) and the optimisation algorithms of the previous section can still be written entirely in terms of incompressible vector fields. Indeed, since for a solenoidal forcing, we must have $\nabla \cdot \chi = 0$ for its correlation matrix function in the sense that $\partial_i \chi_{ij} = 0$ and $\partial_j \chi_{ij} = 0$, the right hand side of the state equation (A11) will automatically be solenoidal, such that the PDE constraint on $u = \mathbb{P}[v]$ can be written as

$$\begin{cases} \partial_t u + \mathbb{P}[(u \cdot \nabla) u] - \Delta u = \chi * p, \\ u(\cdot, -T) = 0. \end{cases} \quad (\text{D9})$$

Similar to the discussion in section C 5, we can see that it is only the solenoidal part of the control p that enters the whole problem and in particular the action functional $S[p] = \frac{1}{2} \int_{-T}^0 dt (p, \chi * p)_{L^2(\Omega, \mathbb{R}^3)}$, since the convolution with χ will project $\hat{p}(k)$ onto k^\top in Fourier space. As for the adjoint equation, all observable quantities can only depend on $u = \mathbb{P}[v]$, such that the final condition for $z(\cdot, 0)$ can be written as

$$z(\cdot, 0) = -\mathbb{P} \left[\frac{\delta O^\top}{\delta u} \Big|_{u(\cdot, 0)} \{ \mathcal{F} + \mu (O[u[p](\cdot, 0)] - a) \} \right] \quad (\text{D10})$$

by the chain rule and is consequently solenoidal. The adjoint equation

$$\partial_t z - \nabla N(u)^\top z = \partial_t z + \mathbb{P} \left[(u \cdot \nabla) z + (\nabla z)^\top u \right] + \Delta z = 0 \quad (\text{D11})$$

will then preserve solenoidality. Summing up the discussion, the instanton equations (C4) at critical points of the action of the incompressible NSE can be written as

$$\begin{cases} \partial_t u_1 + \mathbb{P}[(u_1 \cdot \nabla) u_1] - \Delta u_1 = \chi * p_1, \\ \partial_t p_1 + \mathbb{P}[(u_1 \cdot \nabla) p_1 + (\nabla p_1)^\top u_1] + \Delta p_1 = 0, \\ p_1(\cdot, t = 0) = -\mathbb{P} \left[\frac{\delta O^\top}{\delta u} \Big|_{u_1(0)} \mathcal{F}_1 \right], \end{cases} \quad (\text{D12})$$

with $\nabla \cdot u_1 = \nabla \cdot p_1 = 0$.

2. Forcing

Let us now specify the forcing correlation that we chose and elaborate on related implementation details. Imposing statistical homogeneity and isotropy on the forcing, in addition to solenoidality, reduces the possible forms for the correlation function to [17]

$$\chi(x) = f(\|x\|) \text{Id} + \frac{1}{2} \|x\| f'(\|x\|) \left[\text{Id} - \frac{xx^\top}{\|x\|^2} \right], \quad (\text{D13})$$

where the only freedom is in the choice of the scalar function $f: [0, \infty] \rightarrow \mathbb{R}$. Corresponding to the physical picture of energy injection on large scales, we work with the ‘‘Mexican hat’’ choice $f(r) = \chi_0 \exp\{-r^2/2\lambda^2\}$ with a forcing correlation length $\lambda > 0$ roughly the size of the domain. In Cartesian coordinates, the matrix-valued function χ is then given by

$$\chi(x) = \frac{\chi_0}{2\lambda^2} e^{-\frac{\|x\|^2}{2\lambda^2}} \begin{pmatrix} 2\lambda^2 - x_2^2 - x_3^2 & x_1x_2 & x_1x_3 \\ x_1x_2 & 2\lambda^2 - x_1^2 - x_3^2 & x_2x_3 \\ x_1x_3 & x_2x_3 & 2\lambda^2 - x_1^2 - x_2^2 \end{pmatrix} \quad (\text{D14})$$

for this choice of forcing correlation. For the pseudo-spectral NSE DNS and instanton solver, we need the correlation in Fourier space, which is

$$\hat{\chi}(k) = 2^{1/2} \pi^{3/2} \chi_0 \lambda^5 e^{-\frac{1}{2} \lambda^2 \|k\|^2} \begin{pmatrix} k_2^2 + k_3^2 & -k_1k_2 & -k_1k_3 \\ -k_1k_2 & k_1^2 + k_3^2 & -k_2k_3 \\ -k_1k_3 & -k_2k_3 & k_1^2 + k_2^2 \end{pmatrix}. \quad (\text{D15})$$

We observe that the vector $k \in \mathbb{R}^3$ is in the kernel of $\hat{\chi}(k)$, so applying $\hat{\chi}$ will indeed render the output solenoidal. Furthermore, on $k^\perp \subset \mathbb{R}^3$, the matrix acts as the identity times $c_k = 2^{1/2} \pi^{3/2} \chi_0 \lambda^5 \|k\|^2 e^{-\frac{1}{2} \lambda^2 \|k\|^2}$. In the reduced mode representation of the control p , we concretely determine the number of modes $n_{k,\text{eff}}$ by keeping only those modes with $|c_k| > \chi_{\text{tol}}$. As discussed in general in the previous sections, inverting χ consists of discarding the possibly non-zero part of the input vector in Fourier space parallel to k , and dividing the remaining input by c_k .

In the DNS of the stochastic NSE, we need to sample realisations of the Gaussian random vector field η with the prescribed correlation function χ . From the Fourier transform of the correlation in real space, we find

$$\langle \hat{\eta}(k, t) \hat{\eta}^\dagger(k', t') \rangle = (2\pi)^3 \hat{\chi}(k) \delta^{(3)}(k - k') \delta(t - t'), \quad (\text{D16})$$

i.e. except for the trivial conjugation symmetry $\hat{\eta}(-k, t) = \hat{\eta}(k, t)^*$ for real fields, the correlation in Fourier space decouples between different modes for a stationary forcing. In order to sample realisations of $\hat{\eta}(k, t)$, it is, except for a discretisation-dependent normalisation factor, hence enough to generate independent and identically standard complex normally distributed random vectors $Z(k, t) \sim \mathcal{C}\mathcal{N}(0, \text{Id})$ for all appearing $k \in \mathbb{Z}^3$, multiply the result by a ‘‘square root’’ $\hat{\Lambda}(k)$ of the forcing correlation $\hat{\chi}(k) = \hat{\Lambda}(k) \hat{\Lambda}^\dagger(k)$, and enforce conjugation symmetry afterwards. The random field Z can be generated as $Z(k, t) = 2^{-1/2} (Z_r(k, t) + iZ_i(k, t))$ with independent $Z_r(k, t), Z_i(k, t) \sim \mathcal{N}(0, \text{Id})$. For our choice of χ , the linear map $\hat{\Lambda}(k)$ simply corresponds to projecting onto k^\perp and multiplying by $\sqrt{c_k}$. All in all, if the Fast Fourier Transform (FFT) implementation that is used scales the inverse transformation by $1/(n_{x_1} n_{x_2} n_{x_3})$, then the random forcing prior to the symmetrisation step will be given by

$$\hat{\eta}(k, t) = \left(\frac{n_{x_1} n_{x_2} n_{x_3}}{2\Delta t \Delta x_1 \Delta x_2 \Delta x_3} \right)^{1/2} \Lambda(k) (Z_r(k, t) + iZ_i(k, t)). \quad (\text{D17})$$

On a discrete grid in k -space with standard layout $k_i = 0, 1, \dots, n_{x_i}/2 - 1, -n_{x_i}/2, \dots, -1$, the symmetry condition $\hat{\eta}(-k, t) = \hat{\eta}(k, t)^*$ is understood modulo $(n_{x_1}, n_{x_2}, n_{x_3})$, such that in addition to $\hat{\eta}(k_1 = 0, k_2 = 0, k_3 = 0, t)$ being real, the same is also true if any of the k_j is equal to the Nyquist mode. As an example, the symmetry constraints on a two-dimensional 8×8 grid are summarised in figure 5. On all grid points where the field is supposed to be real, the a posteriori symmetrisation of the random field realisations $\hat{\eta}$ has to set the imaginary part to zero and multiply the real part by $\sqrt{2}$ in order to yield the desired covariance. For all other grid points, one needs to identify symmetry partners at k and $-k \bmod (n_{x_1}, n_{x_2}, n_{x_3})$, discard one of the two field values, say $\hat{\eta}(-k, t)$, and set it equal to $\hat{\eta}(k, t)^*$. A more complete description of sampling algorithms for Gaussian random fields using Fourier transforms can be found in [49]. Also note that if the vorticity formulation of the incompressible NSE in terms of $\omega = \nabla \times u$ is used for the DNS, such that

$$\partial_t \omega + \nabla \times (\omega \times u) - \Delta \omega = \sqrt{\varepsilon} (\nabla \times \eta) \quad (\text{D18})$$

and $\hat{u} = ik \times \hat{\omega} / \|k\|^2$, then the procedure outlined above to sample $\hat{\eta}$ only needs to be modified by multiplying $\hat{\eta}$ by an additional factor of $\|k\|$, i.e. $\widehat{\nabla \times \eta}(k, t) \stackrel{\text{law}}{=} \|k\| \hat{\eta}(k, t)$.

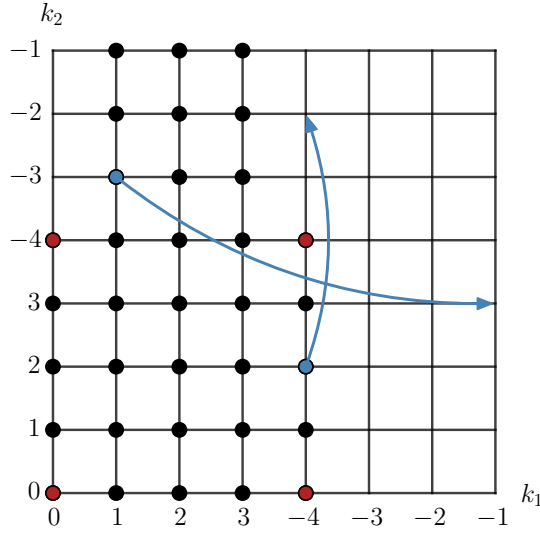


FIG. 5. Two-dimensional 8×8 grid in k -space. The 4 red points are those where the Fourier transform of a real data set is real. These 4 points plus the remaining 30 indicated points form a minimal subset that uniquely determines the entire field, since each of the circled points (k_1, k_2) possesses a partner at indices $(-k_1, -k_2)$ that is determined by $\hat{\eta}(-k_x, -k_y) = \hat{\eta}^*(k_x, k_y)$. Two examples for this symmetry are given by the blue points, with arrows pointing to their respective partner. Note that one effectively mirrors each point (k_1, k_2) at any of the red points to obtain the corresponding mode at $(-k_1, -k_2) \bmod (8, 8)$.

3. Observables and final conditions for the adjoint field

The two observables which we consider in the main text are both one-dimensional, i.e. $d' = 1$ in the general setup of the previous sections, and correspond to the longitudinal and transversal components of the velocity gradient tensor ∇u . Here, we derive the associated final time conditions for the adjoint field. In order to do this, we go back to the formulation in terms of compressible fields introduced in section D 1.

For the first observable, the z -component of the vorticity

$$O_1[u(\cdot, 0)] = (\nabla \times u)_z(x=0, t=0) = \omega_z(0, 0), \quad (\text{D19})$$

we rewrite this function as

$$O_1[v(\cdot, 0)] = (\nabla \times \mathbb{P}[v])_z(x=0, t=0) \quad (\text{D20})$$

and compute, suppressing the time variable,

$$\begin{aligned} \frac{d}{dh} \Big|_{h=0} O_1[v + h\delta v] &= \int_{\Omega} d^3x \delta^{(3)}(x) (\nabla \times \mathbb{P}[\delta v])_z \\ &= \int_{\Omega} d^3x \left(-e_z \times \nabla \delta^{(3)}(x), \mathbb{P}[\delta v] \right) = \left(-e_z \times \nabla \delta_0^{(3)}, \delta v \right)_{L^3(\Omega, \mathbb{R}^3)}, \end{aligned} \quad (\text{D21})$$

where we used partial integration, the self-adjointness of \mathbb{P} as well as the fact that $-e_z \times \nabla \delta_0^{(3)}$ is already solenoidal. Hence, we obtain

$$z_1(x, t=0) = \{ \mathcal{F} + \mu (O[u[p](\cdot, 0)] - a) \} e_z \times \nabla \delta^{(3)}(x) \quad (\text{D22})$$

as the final condition for the adjoint field in the gradient computation of L_A .

For the second observable, the strain

$$O_2[u(\cdot, 0)] = \partial_z u_z(x=0, t=0), \quad (\text{D23})$$

we proceed similarly and compute

$$\frac{d}{dh} \Big|_{h=0} O_2[v + h\delta v] = \int_{\Omega} d^3x \delta^{(3)}(x) \partial_z \mathbb{P}[\delta v]_z = \left(-\mathbb{P} \left[\partial_z \delta_0^{(3)} e_z \right], \delta v \right)_{L^3(\Omega, \mathbb{R}^3)}, \quad (\text{D24})$$

such that

$$z_2(\cdot, t=0) = \{ \mathcal{F} + \mu (O[u[p](\cdot, 0)] - a) \} \mathbb{P} \left[\partial_z \delta_0^{(3)} e_z \right] \quad (\text{D25})$$

for the strain observable.

Both final conditions considered here are highly singular as they involve derivatives of δ distributions, which is due to the fact that we considered single-point observables without any averaging over a finite domain. Of course, these conditions are easy to realise in a pseudo-spectral code in Fourier space, where

$$\hat{z}_1(k, t = 0) = i \{ \mathcal{F} + \mu (O[u[p](\cdot, 0)] - a) \} (-k_y e_x + k_x e_y) \quad (\text{D26})$$

and

$$\hat{z}_2(k, t = 0) = i \{ \mathcal{F} + \mu (O[u[p](\cdot, 0)] - a) \} k_z \left(-\frac{k_x k_z}{\|k\|^2} e_x - \frac{k_y k_z}{\|k\|^2} e_y + \left[1 - \frac{k_z^2}{\|k\|^2} \right] e_z \right). \quad (\text{D27})$$

We directly implemented these final conditions for the 3D code (with additional 2/3 anti-aliasing). However, these conditions are problematic for different numerical schemes. In order to implement these conditions in the finite difference code described below, it is necessary to instead consider

$$\tilde{O}_1[u(\cdot, 0)] = (K_R * \omega_z(\cdot, 0)) (0) \quad (\text{D28})$$

and

$$\tilde{O}_2[u(\cdot, 0)] = (K_R * \partial_z u_z(\cdot, 0)) (0) \quad (\text{D29})$$

with a smooth kernel function K_R in order to average over a ball $B_R(0)$ of radius $R > 0$ centred at the origin and consider the limit $R \rightarrow 0$ as far as it is possible within the finite grid resolution. Details on the resulting final conditions for z in the axisymmetric finite difference code are described below.

4. Numerical implementation and parameters

The spatial discretisation of our full (3+1)-dimensional optimisation code uses a 2/3-dealiased pseudo-spectral method to evaluate all nonlinearities and convolutions via FFTs. For the time discretisation, we use the Heun scheme for both the forward and backward integration. The diffusion term is integrated exactly using an integrating factor in Fourier space in order to avoid the corresponding CFL restriction. All appearing time integrals are discretised using the trapezoidal rule. As discussed in section C 3, we followed the *optimise then discretise* approach, implying that with these time discretisations, the adjoint method does not yield the exact discrete gradient of the discrete action or augmented Lagrangian in our specific example, and gradient-based descent algorithms may get stuck due to this inconsistency. This inconsistency could be reduced in our case by increasing the time resolution. As a result, the achieved accuracy turned out to be sufficient for the PDF scaling estimates.

Since the instanton fields significantly grow in amplitude as $t \rightarrow 0$, we use a non-uniform time parametrisation of the physical interval $[-T, 0]$. We keep this parametrisation fixed, such that the checkpointing algorithm is easily implemented, and choose

$$\varphi : [-1, 0] \rightarrow [-T, 0], \quad \varphi(s) = t = -T \frac{e^{-t\alpha s} - 1}{e^{t\alpha} - 1} \quad (\text{D30})$$

with a constant $t_\alpha > 0$ and a uniform grid in s . While in principle we are interested in solving the minimisation problem on the infinite time interval $T \rightarrow \infty$ in order to characterise the stationary distribution of u , we performed all computations at finite T for this paper and refrained from using a geometric reparametrisation [50, 51]. Instead, the time interval was chosen large enough such that it exceeds the large eddy turnover time T_{LET} at the Reynolds numbers which we considered in DNS of the stochastic NSE.

All parameters of the full three-dimensional computations that have been used to obtain the results shown in the main text are given in table I. All necessary operators for the full 3D Navier-Stokes solver used for this work have been implemented using the CUDA API and are controlled through Python using PyCUDA [52].

Appendix E: Axisymmetric Navier-Stokes instanton implementation

In this section, we include some implementation-related details of a second, explicitly axisymmetric flow solver that has been used in order to compute and stabilise axisymmetric solutions of (D12), as motivated in the main text. In the following, we work in cylindrical coordinates (r, θ, z) with $x_1 = r \cos \theta$, $x_2 = r \sin \theta$, $x_3 = z$. For the axisymmetric instanton computations, we directly used the CS approach as introduced in section B 1, i.e. we only specify a range of Lagrange multipliers \mathcal{F} without penalty, and solve the instanton equations iteratively for fixed values of \mathcal{F} .

TABLE I. Parameters of the full (3+1)-dimensional minimisation of L_A , as defined in (C1), for the incompressible 3D NSE (D1) with the L-BFGS method as described in algorithm (6).

Parameter	Explanation	Typical value
T	Time interval $[-T, 0]$	1
Ω	Periodic domain	$[0, 2\pi]^3$
u_0	Fixed initial condition for u	0
χ_0	Default forcing strength in (D14)	1
λ	Forcing correlation length in (D14)	1
n_x, n_y, n_z	Spatial resolution	128
n_t	Temporal resolution	512
t_α	Stretching factor for time in (D30)	3
χ_{tol}	Threshold for reduced modes	10^{-14}
μ	Penalty parameters	5, ..., 400
m	Number of stored updates	5
δ	Error tolerance for gradient norm	$5 \cdot 10^{-4}$
σ_{init}	Initial step size for line search	1
σ_{min}	Minimum step size for line search	$5 \cdot 10^{-3}$
β	Backtracking fraction	0.5
c	Sufficient decrease constant in (C12)	10^{-2}
\tilde{c}	Angle condition constant in (C20)	10^{-4}

1. Axisymmetric instanton equations and boundary conditions

We begin by noting that, while the forward and backward evolution equations for u_I and p_I in (D12) are invariant under any rotation in \mathbb{R}^3 , the vorticity and strain observables which we consider reduce this symmetry to axial symmetry under rotation around the z -axis. It is hence natural to search for axisymmetric solutions of (D12), which, however, are not guaranteed to yield the global minimum of the corresponding optimisation problem. In order to make the symmetry of the final conditions for p_I more transparent, we introduce, as indicated in section D 3, a smooth Gaussian convolution kernel

$$K_R(x) = (2\pi R^2)^{-3/2} \exp\left\{-\frac{\|x\|^2}{2R^2}\right\} \quad (\text{E1})$$

with radial extent $R > 0$ and consider the convolved observables (D28), (D29), which leads to the final conditions

$$p_I(r, \theta, z, t = 0) = -\mathcal{F}_I (2\pi R^2)^{-3/2} R^{-2} r \exp\left\{-\frac{r^2 + z^2}{2R^2}\right\} e_\theta \quad (\text{E2})$$

for the p -field in the vorticity case and

$$(\nabla \times p_I)(r, \theta, z, t = 0) = -\mathcal{F}_I (2\pi R^2)^{-3/2} R^{-4} r z \exp\left\{-\frac{r^2 + z^2}{2R^2}\right\} e_\theta \quad (\text{E3})$$

for the curl of the p -field in the strain case, where e_θ is the unit vector in θ -direction and axial symmetry is apparent.

The axisymmetric instanton equations (D12) in cylindrical coordinates are given by

$$\begin{cases} D_t u_r - \frac{1}{r} u_\theta^2 + \partial_r P - L u_r = (\chi * p)_r, \\ D_t u_\theta + \frac{1}{r} u_r u_\theta - L u_\theta = (\chi * p)_\theta, \\ D_t u_z + \partial_z P - \left[\frac{1}{r} \partial_r (r \partial_r \cdot) + \partial_{zz}\right] u_z = (\chi * p)_z, \\ D_t p_r - \frac{1}{r} u_\theta p_\theta + u_r \partial_r p_r + u_\theta \partial_r p_\theta + u_z \partial_r p_z + \partial_r Q + L p_r = 0, \\ D_t p_\theta + \frac{1}{r} (2u_\theta p_r - u_r p_\theta) + L p_\theta = 0, \\ D_t p_z + u_r \partial_z p_r + u_\theta \partial_z p_\theta + u_z \partial_z p_z + \partial_z Q + \left[\frac{1}{r} \partial_r (r \partial_r \cdot) + \partial_{zz}\right] p_z = 0, \end{cases} \quad (\text{E4})$$

where

$$D_t = \partial_t + u_r \partial_r + u_z \partial_z \quad (\text{E5})$$

is the axisymmetric convective derivative. Here, L denotes the elliptic operator

$$L = \frac{1}{r} \partial_r (r \partial_r \cdot) + \partial_{zz} - \frac{1}{r^2} \quad (\text{E6})$$

originating from the vector Laplacian in cylindrical coordinates, and the fields have to satisfy the incompressibility constraint

$$\partial_r u_r + \frac{1}{r} u_r + \partial_z u_z = 0, \quad \partial_r p_r + \frac{1}{r} p_r + \partial_z p_z = 0, \quad (\text{E7})$$

which is enforced by the pressures P and Q . In order to conveniently incorporate the incompressibility constraint, we use streamfunctions with

$$u = u(r, z) = \nabla \times (\psi(r, z) e_\theta) + u_\theta(r, z) e_\theta, \quad p = p(r, z) = \nabla \times (\phi(r, z) e_\theta) + p_\theta(r, z) e_\theta. \quad (\text{E8})$$

The streamfunctions ψ and ϕ determine the r and z components of the fields via

$$u_r = -\partial_z \psi, \quad u_z = \frac{1}{r} \partial_r (r \psi), \quad p_r = -\partial_z \phi, \quad p_z = \frac{1}{r} \partial_r (r \phi), \quad (\text{E9})$$

and can be computed from the vorticities $\omega = \nabla \times u$ and $\sigma = \nabla \times p$ by solving

$$\omega_\theta = -L\psi, \quad \sigma_\theta = -L\phi. \quad (\text{E10})$$

Hence, taking u_θ and ω_θ as well as p_θ and ρ_θ as the independent dynamical variables, the instanton equations in vorticity-streamfunction formulation are

$$\begin{cases} D_t u_\theta + \frac{1}{r} u_r u_\theta - L u_\theta = [\chi * p]_\theta, \\ D_t \omega_\theta - \frac{1}{r} u_r \omega_\theta - \frac{1}{r} \partial_z (u_\theta^2) - L \omega_\theta = [(\nabla \times \chi) * p]_\theta, \\ D_t p_\theta + \frac{1}{r} (2u_\theta p_r - u_r p_\theta) + L p_\theta = 0, \\ D_t \sigma_\theta - \frac{1}{r} \partial_z (u_\theta p_\theta) + \partial_z u_\theta \partial_r p_\theta - \partial_r u_\theta \partial_z p_\theta \\ \quad + 2(\omega_\theta + 2\partial_r u_z) \partial_r p_r + \frac{2}{r} \partial_r u_z p_r + (2\partial_z u_z + \frac{u_r}{r}) (2\partial_z p_r - \sigma_\theta) + L \sigma_\theta = 0, \end{cases} \quad (\text{E11})$$

where the r and z components of u and p have to be computed by solving (E10). The final conditions for p are (E2) and (E3) for the averaged observables that we consider in the following, and in particular, we have $\sigma_\theta(t=0) = 0$ for the vorticity observable and $p_\theta(t=0) = 0$ for the strain observable. The instanton equations (E11), to be solved on the time interval $[-T, 0]$ in the r - z -plane $[0, r_{\max}] \times [-z_{\max}, z_{\max}]$, have to be supplemented by the following spatial boundary conditions: At the radial boundaries $r=0$ and $r=r_{\max}$, all fields obey homogeneous Dirichlet boundary conditions (except for the z components of the appearing vector fields at $r=0$, which do not necessarily vanish there). In z , the boundary conditions are periodic in $[-z_{\max}, z_{\max}]$. We impose additional reflection symmetries at $z=0$ in accordance with the equations of motion, which enables us to solve (E11) only in the upper half of the domain with $z \in [0, z_{\max}]$. Even fields with respect to reflection at $z=0$ thus have to fulfil homogeneous Neumann boundary conditions at $z=0$ and $z=z_{\max}$, whereas odd fields with respect to reflection at $z=0$ obey homogeneous Dirichlet boundary conditions in z . Even symmetry can be imposed for u_r , u_θ , ω_z , p_r , p_θ and σ_z , and odd symmetry for u_z , ω_r , ω_θ , ψ , p_z , σ_r , σ_θ and ϕ .

2. Spatio-temporal discretisation

Based on the numerical approach of [33] for the simulation of axisymmetric Euler flows, we use standard symmetric second order finite differences for all appearing spatial derivatives and discretise the spatial domain on a regularly spaced grid of size $(n_r + 1) \times (n_z + 1)$ in $[0, r_{\max}] \times [0, z_{\max}]$ with grid spacing $\Delta r = r_{\max}/n_r$ and $\Delta z = z_{\max}/n_z$.

For this spatial discretisation, the r and z components of the u and p fields at each instant in time are determined by first solving

$$\begin{aligned} -(L\psi)_{ij}^{(n)} = & - \left(\frac{\psi_{i+1,j}^{(n)} - 2\psi_{i,j}^{(n)} + \psi_{i-1,j}^{(n)}}{\Delta r^2} + \frac{1}{r_i} \frac{\psi_{i+1,j}^{(n)} - \psi_{i-1,j}^{(n)}}{2\Delta r} \right. \\ & \left. - \frac{1}{r_i^2} \psi_{i,j}^{(n)} + \frac{\psi_{i,j+1}^{(n)} - 2\psi_{i,j}^{(n)} + \psi_{i,j-1}^{(n)}}{\Delta z^2} \right) = \omega_{\theta,ij}^{(n)}, \end{aligned} \quad (\text{E12})$$

for $i = 1, \dots, n_r - 1$ and $j = 1, \dots, n_z - 1$ with Dirichlet 0 boundary conditions at $i=0$, $i=n_r$ or $j=0$ and $j=n_z$ for $\psi_{ij}^{(n)}$. Here the upper index indicates fields at time t_n and lower indices denote the spatial position

$r_i = i\Delta r$, $z_j = j\Delta z$. Once we have determined $\psi^{(n)}$, which is discussed below, we can determine $u_r^{(n)}$ and $u_z^{(n)}$ as

$$u_{r,ij}^{(n)} = -\frac{\psi_{i,j+1}^{(n)} - \psi_{i,j-1}^{(n)}}{2\Delta z}, \quad u_{z,ij}^{(n)} = \frac{\psi_{i+1,j}^{(n)} - \psi_{i-1,j}^{(n)}}{2\Delta r} + \frac{1}{r_i} \psi_{ij}^{(n)}, \quad (\text{E13})$$

where, for $j = 0$ and $j = n_z$, $\psi_{i,j+1}^{(n)}$ and $\psi_{i,j-1}^{(n)}$ are reflected to fulfil the imposed odd symmetry in z . For the time discretisation of all evolution equations in (E11), we use the Leapfrog scheme. Suppose for now for notational simplicity that the time interval $[-T, 0]$ is discretised equidistantly with $n_t + 1$ points at distance $\Delta t = T/n_t$. In the actual instanton computations, we again use the exponentially stretched time parametrisation (D30), but it is straightforward to formulate the following discretisations for a uniform grid in $s \in [-1, 0]$ and fields $\tilde{u} = u \circ \phi$, $\tilde{\omega} = \omega \circ \phi$ and so forth. In order to avoid the severe restriction on the permitted Δt that would otherwise arise from the diffusion CFL condition, we choose a Crank-Nicolson like, semi-implicit discretisation $[Lh^{(n+1)} + Lh^{(n-1)}]/2$ for all four diffusion terms in (E11). Concretely, in order to determine $u_\theta^{(n+1)}$ given all fields at times $t^{(n-1)}$ and $t^{(n)}$, we discretise

$$\begin{aligned} & \frac{u_{\theta,ij}^{(n+1)} - u_{\theta,ij}^{(n-1)}}{2\Delta t} + u_{r,ij}^{(n)} \frac{u_{\theta,i+1,j}^{(n)} - u_{\theta,i-1,j}^{(n)}}{2\Delta r} + u_{z,ij}^{(n)} \frac{u_{\theta,i,j+1}^{(n)} - u_{\theta,i,j-1}^{(n)}}{2\Delta z} \\ & + \frac{1}{r_i} u_{r,ij}^{(n)} \frac{u_{\theta,i+1,j}^{(n)} + u_{\theta,i-1,j}^{(n)}}{2} - \frac{1}{2} \left[\left(Lu_\theta^{(n+1)} \right)_{ij} + \left(Lu_\theta^{(n-1)} \right)_{ij} \right] = [\chi * p]_{\theta,ij}^{(n)}, \end{aligned} \quad (\text{E14})$$

such that a Helmholtz equation

$$u_{\theta,ij}^{(n+1)} - \Delta t \left(Lu_\theta^{(n+1)} \right)_{ij} = r_{ij} \quad (\text{E15})$$

with an appropriate r_{ij} as determined by (E14) needs to be solved to update u_θ . All other equations in (E11) are treated similarly.

Both (E12) and (E15) are special cases of a discretisation of the (noncritical) Helmholtz equation

$$\begin{cases} [a \text{Id} - bL]u = f, & L = \left[\frac{1}{r} \partial_r (r \partial_r \cdot) - \frac{1}{r^2} + \partial_{zz} \right] \text{ in } [0, r_{\max}] \times [0, z_{\max}], \\ u(r = 0, \cdot) = u(r = r_{\max}, \cdot) = 0, \\ u(\cdot, z = 0) = u(\cdot, z = z_{\max}) = 0 \text{ or } \partial_z u(\cdot, z = 0) = \partial_z u(\cdot, z = z_{\max}) = 0, \end{cases} \quad (\text{E16})$$

with constants $a, b > 0$. We use a multigrid solver for this equation with a Gauss-Seidel smoother with one iteration per grid, full-weighting restrictions, bilinear interpolation for the prolongation and W-cycles for the recursion (see e.g. [34]), in order to solve the discretised Helmholtz equations to an accuracy of $\epsilon_{\text{mgrid}} = 10^{-12}$.

Von Neumann stability analysis of the Leapfrog scheme for the linear advection equation shows the existence of the so-called computational mode, leading to even-odd-oscillations in the time domain at a frequency of $2/\Delta t$ of the scheme due to decoupling of directly adjacent fields in time. In order to mitigate this problem, we added a Robert-Asselin-Williams time filter with strength 10^{-2} to the scheme [53–55].

3. Fast evaluation of polar convolutions

Here, we discuss how to efficiently evaluate the convolutions $(\chi * p)_\theta$ and $(\chi * \sigma)_\theta$ which appear on the RHS of the forward equation for u , as well as $(\chi * p)_r$ and $(\chi * p)_z$, which are additionally needed for the computation of the action integral (which we discretise in real space using the trapezoidal rule in space and time). In order to speed up the naive $\mathcal{O}(n^6)$ scaling of a direct evaluation of a three-dimensional convolution on a grid with n points in each direction, the usual approach for suitable domains is to employ the convolution theorem

$$(f * g)(x) = \int_{\mathbb{R}^3} d^3 k \hat{f}(k) \hat{g}(k) e^{i(k,x)_3} \quad (\text{E17})$$

for $\Omega = \mathbb{R}^3$ and $f, g : \Omega \rightarrow \mathbb{R}$ integrable, or its discrete equivalent using Fourier series on bounded, periodic domains. By virtue of the FFT, this reduces the cost to compute a three-dimensional convolution to $\mathcal{O}(n^3 \log^3 n)$. Since we consider axisymmetric fields as well as an isotropic forcing and the convolved fields will thus be axisymmetric as well, a valid option to compute the necessary convolutions in our setting would be to first extrapolate all polar fields onto a full three-dimensional grid. Afterwards, we could compute the convolutions with χ via 3D FFTs, and then obtain the components of the result in cylindrical coordinates

in the r - z -plane e.g. in the $x \geq 0, y = 0$ half-plane where $(\chi * p)_r = (\chi * p)_x$ and $(\chi * p)_\theta = (\chi * p)_y$. It is, however, possible to directly evaluate the convolutions in cylindrical coordinates, which is in particular cheaper for a large-scale forcing. The associated costs scale as $\mathcal{O}(n_{\text{Bz}} n^2 \log n)$, where n_{Bz} is the (small) number of zeros of various Bessel functions appearing in the polar convolutions, as detailed below. For a comprehensive introduction to the evaluation of Fourier transforms and convolutions in polar coordinates, see [56].

The Fourier transform of a scalar function f in cylindrical coordinates (r, θ, z) can in general be expressed as

$$\begin{aligned} \hat{f}(k_r, \theta_k, k_z) &= \int_0^\infty dr \int_0^{2\pi} d\theta \int_{-\infty}^\infty dz r f(r, \theta, z) e^{-ik_z z} e^{-ik_r r \cos(\theta_k - \theta)} \\ &= \sum_{l=-\infty}^\infty 2\pi i^{-l} \mathbb{H}_l[\tilde{f}_l](k_r, k_z) e^{il\theta_k} =: \sum_{l=-\infty}^\infty \hat{f}_l(k_r, k_z) e^{il\theta_k}, \end{aligned} \quad (\text{E18})$$

where

$$\tilde{f}_m(r, \theta, k_z) = \int_{-\infty}^\infty dz f(r, \theta, z) e^{-ik_z z} = \sum_{m=-\infty}^\infty \tilde{f}_m(r, k_z) e^{im\theta} \quad (\text{E19})$$

is the partial Fourier transform in z direction, which we then expanded in an angular Fourier series with coefficients

$$\tilde{f}_m(r, k_z) = \frac{1}{2\pi} \int_0^{2\pi} d\theta \tilde{f}(r, \theta, k_z) e^{-im\theta}. \quad (\text{E20})$$

Finally, inserting the expansion

$$e^{-ik_r r \cos(\theta_k - \theta)} = \sum_{l=-\infty}^\infty i^{-l} J_l(k_r r) e^{-il\theta} e^{il\theta_k} \quad (\text{E21})$$

in terms of Bessel functions J_l of the first kind of order l resulted in the second line of (E18), which involves l -th order Hankel transforms, defined via

$$\mathbb{H}_l[h](k_r) := \int_0^\infty dr r h(r) J_l(k_r r) \quad (\text{E22})$$

for functions $h : [0, \infty) \rightarrow \mathbb{R}$ for which the integral exists. Also note that for negative integer orders, the Bessel functions of the first kind fulfil $J_{-l} = (-1)^l J_l$, $l \in \mathbb{N}$. In summary, computing the Fourier transform of a function in cylindrical coordinates consists of three steps: First, perform a Fourier transform in z , then a Fourier series decomposition in θ , followed by radial Hankel transforms of order l for each term of the angular series. In the special case that f is axisymmetric, the Fourier transform (E18) reduces to

$$\hat{f}(k_r, k_z) = 2\pi \mathbb{H}_0[\tilde{f}](k_r, k_z). \quad (\text{E23})$$

Since the Hankel transform is an involution for all real $l \geq -1/2$ and in particular for all $l \in \mathbb{Z}$, inverse Fourier transforms in cylindrical coordinates can analogously be evaluated by performing an ordinary inverse transform in z and Hankel transforms of order l times $i^l/2\pi$ on all angular coefficients, such that

$$f(r, \theta, z) = \sum_{l=-\infty}^\infty \tilde{f}_l(r, z) e^{il\theta} = \sum_{l=-\infty}^\infty e^{il\theta} \frac{i^l}{2\pi} \mathbb{H}_l[\text{IFT}_z[\hat{f}_l]](r, z). \quad (\text{E24})$$

Now, we elaborate on how to use the polar Fourier transform that has just been introduced for the convolution of χ and p in practice. Let us focus on the example of evaluating $(\chi * p)_\theta$ for concreteness. In order to avoid integrations over unit vectors in cylindrical coordinates, we compute $(\chi * p)_\theta(r, z)$ as

$$(\chi * p)_\theta(r, z) = [\chi_{yx} * p_x + \chi_{yy} * p_y + \chi_{yz} * p_z](x = r, y = 0, z) \quad (\text{E25})$$

using Cartesian components. For the three individual scalar convolutions that need to be evaluated, we first analytically compute the Fourier transforms of the components of χ (if possible) and expand them in an

angular Fourier series. For the specific choice (D14) for the forcing covariance, we obtain e.g.

$$\begin{aligned}\hat{\chi}_{yx}(k_r, \theta_k, k_z) &= -2^{1/2} \pi^{3/2} \chi_0 \lambda^5 e^{-\frac{1}{2} \lambda^2 (k_r^2 + k_z^2)} k_r^2 \sin \theta_k \cos \theta_k \\ &= i 2^{-3/2} \pi^{3/2} \chi_0 \lambda^5 e^{-\frac{1}{2} \lambda^2 (k_r^2 + k_z^2)} k_r^2 \left(e^{2i\theta_k} - e^{-2i\theta_k} \right) \\ &= \hat{\chi}_{yx,2} e^{2i\theta_k} + \hat{\chi}_{yx,-2} e^{-2i\theta_k},\end{aligned}\quad (\text{E26})$$

$$\begin{aligned}\hat{\chi}_{yy}(k_r, \theta_k, k_z) &= 2^{1/2} \pi^{3/2} \chi_0 \lambda^5 e^{-\frac{1}{2} \lambda^2 (k_r^2 + k_z^2)} (k_r^2 \cos^2 \theta_k + k_z^2) \\ &= 2^{-3/2} \pi^{3/2} \chi_0 \lambda^5 e^{-\frac{1}{2} \lambda^2 (k_r^2 + k_z^2)} \left(k_r^2 e^{2i\theta_k} + k_r^2 e^{-2i\theta_k} + (2k_r^2 + 4k_z^2) e^{0i\theta_k} \right) \\ &= \hat{\chi}_{yy,2} e^{2i\theta_k} + \hat{\chi}_{yy,-2} e^{-2i\theta_k} + \hat{\chi}_{yy,0} e^{0i\theta_k},\end{aligned}\quad (\text{E27})$$

$$\begin{aligned}\hat{\chi}_{yz}(k_r, \theta_k, k_z) &= i 2^{-1/2} \pi^{3/2} \chi_0 \lambda^5 e^{-\frac{1}{2} \lambda^2 (k_r^2 + k_z^2)} k_r k_z \left(e^{i\theta_k} - e^{-i\theta_k} \right) \\ &= \hat{\chi}_{yz,1} e^{i\theta_k} + \hat{\chi}_{yz,-1} e^{-i\theta_k}.\end{aligned}\quad (\text{E28})$$

Starting from the fields $p_r(r, z)$, $p_\theta(r, z)$ and $p_z(r, z)$ which will numerically be available on a regular grid in $[0, r_{\max}] \times [0, z_{\max}]$, we first extend all components of p onto $[0, r_{\max}] \times [-z_{\max}, z_{\max}]$ by reflection symmetry and perform a Fourier transform in z via FFT to obtain $\tilde{p}_r(r, k_z)$, $\tilde{p}_\theta(r, k_z)$ and $\tilde{p}_z(r, k_z)$ at regularly spaced Fourier modes $k_z = 0, \dots, n_z/2 - 1, -n_z/2, \dots, -1$. Since χ decays exponentially with k_z^2 , it then suffices to perform the computations described in the following on a reduced grid only for modes with $|k_z| < k_{z,\max} \ll n_z/2$. From these fields, we compute

$$\tilde{p}_x(r, \theta, k_z) = \tilde{p}_r(r, k_z) \cos \theta - \tilde{p}_\theta(r, k_z) \sin \theta = \frac{1}{2} \left\{ (\tilde{p}_r + i\tilde{p}_\theta) e^{i\theta} + (\tilde{p}_r - i\tilde{p}_\theta) e^{-i\theta} \right\} \quad (\text{E29})$$

$$\tilde{p}_y(r, \theta, k_z) = \tilde{p}_r(r, k_z) \sin \theta + \tilde{p}_\theta(r, k_z) \cos \theta = \frac{1}{2} \left\{ (\tilde{p}_\theta - i\tilde{p}_r) e^{i\theta} + (\tilde{p}_\theta + i\tilde{p}_r) e^{-i\theta} \right\} \quad (\text{E30})$$

$$\tilde{p}_z(r, \theta, k_z) = \tilde{p}_z(r, k_z) e^{0i\theta}, \quad (\text{E31})$$

or, after numerically evaluating Hankel transforms of 0th and 1st order as detailed below, all appearing Fourier coefficients $\hat{p}_{x,1}(k_r, k_z)$, $\hat{p}_{x,-1}(k_r, k_z)$, $\hat{p}_{y,1}(k_r, k_z)$, $\hat{p}_{y,-1}(k_r, k_z)$ and $\hat{p}_{z,0}(k_r, k_z)$ where a non-uniform grid in k_r will turn out to be useful. Then, we calculate the pointwise multiplication of $\hat{\chi}_{yx}$ and \hat{p}_x and so on, and arrange the results again in terms of angular Fourier series

$$\hat{\chi}_{yx} \hat{p}_x = \hat{\chi}_{yx,2} \hat{p}_{x,1} e^{3i\theta_k} + \hat{\chi}_{yx,-2} \hat{p}_{x,-1} e^{-3i\theta_k} + \hat{\chi}_{yx,2} \hat{p}_{x,-1} e^{i\theta_k} + \hat{\chi}_{yx,-2} \hat{p}_{x,1} e^{-i\theta_k}, \quad (\text{E32})$$

$$\begin{aligned}\hat{\chi}_{yy} \hat{p}_y &= \hat{\chi}_{yy,2} \hat{p}_{y,1} e^{3i\theta_k} + \hat{\chi}_{yy,-2} \hat{p}_{y,-1} e^{-3i\theta_k} + (\hat{\chi}_{yy,2} \hat{p}_{y,-1} + \hat{\chi}_{yy,0} \hat{p}_{y,1}) e^{i\theta_k} \\ &\quad + (\hat{\chi}_{yy,-2} \hat{p}_{y,1} + \hat{\chi}_{yy,0} \hat{p}_{y,-1}) e^{-i\theta_k},\end{aligned}\quad (\text{E33})$$

$$\hat{\chi}_{yz} \hat{p}_z = \hat{\chi}_{yz,1} \hat{p}_{z,0} e^{i\theta_k} + \hat{\chi}_{yz,-1} \hat{p}_{z,0} e^{-i\theta_k}. \quad (\text{E34})$$

According to (E24), we then need to compute Hankel transforms of order 1 and 3 on the coefficients, zero-pad all fields to the full k_z grid again and perform an IFFT in z , plug in $\theta = 0$ in the end and add all contributions in order to obtain the result $(\chi * p)_\theta$. The efficiency of the proposed method hence depends on two ingredients: The fact that only a small number of angular modes appears for our choice of χ , which limits the number of different order Hankel transforms that have to be computed, plus an efficient implementation of the Hankel transform evaluations themselves.

Following [35, 36, 57], we use the following series expansion with fast convergence to compute the *inverse* Hankel transform from Fourier space to real space:

$$\tilde{f}_l(r, k_z) \approx \frac{i^l}{2\pi} \frac{2}{r_{\max}^2} \sum_{m=1}^{n_{Bz}} \frac{J_n(j_{l,m} r / r_{\max})}{(J'_l(j_{l,m}))^2} \hat{f}_l(j_{l,m} / r_{\max}, k_z), \quad (\text{E35})$$

where $j_{l,m}$ denotes the m -th zero (in ascending order) of the Bessel function J_l . For this, we need to evaluate the *forward* Hankel transforms of the components of p at $n_{Bz} \ll n_r$ points $j_{l,m} / r_{\max}$ for all angular modes l that appear in the products (E32) to (E34). We calculate these forward transforms of the components of p with a straightforward quadrature of (E22), specifically with the trapezoidal rule as in [36].

4. Numerical implementation and parameters

For the axisymmetric instanton equations, a simplified version of the gradient descent algorithm 4 turned out to be sufficient. We only specify Lagrange multipliers \mathcal{F} without penalty, perform updates (C11) with fixed step sizes that are reduced by a factor β whenever an oscillation of $O[u[p](\cdot, 0)]$ between iterations

TABLE II. Parameters of the axisymmetric (2+1)-dimensional solver of the instanton equations (E11) using a forward-backward iteration at fixed values of \mathcal{F} .

Parameter	Explanation	Typical value
T	Time interval $[-T, 0]$	1
r_{\max}	Radial domain $[0, r_{\max}]$	π
z_{\max}	z -domain $[-z_{\max}, z_{\max}]$	π
u_0	Fixed initial condition for u	0
χ_0	Default forcing strength in (D14)	1
λ	Forcing correlation length in (D14)	1
n_r, n_z	Resolution of $[0, r_{\max}] \times [0, z_{\max}]$	256
n_t	Temporal resolution	1024
t_α	Stretching factor for time in (D30)	3
$n_{z,\text{red}}$	Reduced number of z modes	10
n_{Bz}	# of Bessel zeros for convolutions	10
R	Width of the final conditions for p_1	Δr
$\tilde{\beta}$	Step size reduction factor	0.8
δ	Threshold for stopping in (E36)	$5 \cdot 10^{-3}$

is detected, and stop iterating once the relative change of $O[u[p](\cdot, 0)]$ between iterations drops below a threshold δ according to

$$\left| \frac{O[u[p^{(k)}](\cdot, 0)] - O[u[p^{(k-1)}](\cdot, 0)]}{\sigma^{(k-1)} O[u[p^{(k-1)}](\cdot, 0)]} \right| < \delta. \quad (\text{E36})$$

The numerical parameters for the axisymmetric solver that have been used to obtain the results of the main paper are summarised in table II. Regarding the concrete implementation, the code that has been written and used for this task consists of Fortran 90 subroutines for the Leapfrog steps and the multigrid solver that are called in Python via F2PY [58].

-
- [1] E. Novikov, *Fluid Dynamics Research* **12**, 107 (1993).
 - [2] R. C. Y. Mui, D. G. Dommermuth, and E. A. Novikov, *Physical Review E* **53**, 2355 (1996).
 - [3] P. K. Yeung, X. M. Zhai, and K. R. Sreenivasan, *Proceedings of the National Academy of Sciences* **112**, 12633 (2015).
 - [4] D. Buaria, A. Pumir, E. Bodenschatz, and P. K. Yeung, *New Journal of Physics* **21**, 043004 (2019).
 - [5] T. P. Sapsis, *Annual Review of Fluid Mechanics* **53**, 85 (2021).
 - [6] T. Grafke, R. Grauer, and T. Schäfer, *Journal of Physics A: Mathematical and Theoretical* **48**, 333001 (2015).
 - [7] M. I. Freidlin and A. D. Wentzell, *Random perturbations of dynamical systems*, Vol. 260 (Springer, 2012).
 - [8] T. Grafke and E. Vanden-Eijnden, *Chaos: An Interdisciplinary Journal of Nonlinear Science* **29**, 063118 (2019).
 - [9] E. Balkovsky, G. Falkovich, I. Kolokolov, and V. Lebedev, *Physical Review Letters* **78**, 1452 (1997).
 - [10] A. I. Chernykh and M. G. Stepanov, *Physical Review E* **64**, 026306 (2001).
 - [11] T. Grafke, R. Grauer, T. Schäfer, and E. Vanden-Eijnden, *EPL (Europhysics Letters)* **109**, 34003 (2015).
 - [12] B. Meerson, E. Katzav, and A. Vilenkin, *Physical Review Letters* **116**, 070601 (2016).
 - [13] G. Dematteis, T. Grafke, M. Onorato, and E. Vanden-Eijnden, *Physical Review X* **9**, 041057 (2019).
 - [14] S. Tong, E. Vanden-Eijnden, and G. Stadler, *arXiv preprint arXiv:2007.13930* (2020).
 - [15] T. Lestang, F. Bouchet, and E. Lévêque, *Journal of Fluid Mechanics* **895**, A19 (2020).
 - [16] M. Janas, A. Kamenev, and B. Meerson, *Phys. Rev. E* **94**, 032133 (2016).
 - [17] H. P. Robertson, *Mathematical Proceedings of the Cambridge Philosophical Society* **36**, 209 (1940).
 - [18] T. Grafke, R. Grauer, and T. Schäfer, *Journal of Physics A: Mathematical and Theoretical* **46**, 062002 (2013).
 - [19] G. Falkovich and V. Lebedev, *Phys. Rev. E* **83**, 045301 (2011).
 - [20] A. Migdal, *arXiv preprint arXiv:2103.02065* (2021).
 - [21] D. S. Agafontsev, E. A. Kuznetsov, and A. A. Mailybaev, *arXiv preprint arXiv:2106.09176* (2021).
 - [22] S. Machlup and L. Onsager, *Phys. Rev.* **91**, 1512 (1953).
 - [23] H. Touchette, *Physics Reports* **478**, 1 (2009).
 - [24] T. Schorlepp, T. Grafke, and R. Grauer, *Journal of Physics A: Mathematical and Theoretical* **54**, 235003 (2021).
 - [25] J. Duchon and R. Robert, *Nonlinearity* **13**, 249 (1999).
 - [26] A. J. Majda and A. L. Bertozzi, *Vorticity and Incompressible Flow*, Cambridge Texts in Applied Mathematics (Cambridge University Press, 2001).
 - [27] G. Batchelor, *An introduction to fluid dynamics* (Cambridge University Press, 2000).
 - [28] F. Tröltzsch, *Optimal control of partial differential equations: theory, methods, and applications*, Vol. 112 (American Mathematical Soc., 2010).
 - [29] R. Herzog and K. Kunisch, *GAMM-Mitteilungen* **33**, 163 (2010).
 - [30] M. R. Hestenes, *Journal of optimization theory and applications* **4**, 303 (1969).

- [31] M. Alqahtani and T. Grafke, *Journal of Physics A: Mathematical and Theoretical* **54**, 175001 (2021).
- [32] J. Nocedal and S. J. Wright, *Numerical optimization* (Springer Science+ Business Media, 2006).
- [33] R. Grauer and T. C. Sideris, *Physical Review Letters* **67**, 3511 (1991).
- [34] U. Trottenberg, C. W. Oosterlee, and A. Schuller, *Multigrid* (Elsevier, 2000).
- [35] H. Fisk Johnson, *Computer Physics Communications* **43**, 181 (1987).
- [36] O. Melchert, M. Wollweber, and B. Roth, *Biomedical Physics & Engineering Express* **4**, 025025 (2018).
- [37] T. Grafke, R. Grauer, and S. Schindel, *Communications in Computational Physics* **18**, 577 (2015).
- [38] M. Wilczek and C. Meneveau, *Journal of Fluid Mechanics* **756**, 191 (2014).
- [39] L. Lu and C. R. Doering, *Indiana University Mathematics Journal* , 2693 (2008).
- [40] F. Moisy and J. Jiménez, *Journal of Fluid Mechanics* **513**, 111 (2004).
- [41] K. P. Iyer, J. Schumacher, K. R. Sreenivasan, and P. K. Yeung, *New Journal of Physics* **21**, 033016 (2019).
- [42] E. B. Wilson, *Journal of the American Statistical Association* **22**, 209 (1927).
- [43] L. D. Brown, T. T. Cai, and A. DasGupta, *Statistical science* **16**, 101 (2001).
- [44] K. Kleineberg and R. Friedrich, *Phys. Rev. E* **87**, 033007 (2013).
- [45] R. Benzi, L. Biferale, G. Ruiz-Chavarria, S. Ciliberto, and F. Toschi, *Physics of Fluids* **11**, 2215 (1999).
- [46] J. Schumacher, K. R. Sreenivasan, and V. Yakhot, *New Journal of Physics* **9**, 89 (2007).
- [47] J. Friedrich, G. Margazoglou, L. Biferale, and R. Grauer, *Phys. Rev. E* **98**, 023104 (2018).
- [48] R.-E. Plessix, *Geophysical Journal International* **167**, 495 (2006).
- [49] A. Lang and J. Potthoff, *Monte Carlo Methods Appl.* **17**, 195 (2011).
- [50] M. Heymann and E. Vanden-Eijnden, *Communications on Pure and Applied Mathematics: A Journal Issued by the Courant Institute of Mathematical Sciences* **61**, 1052 (2008).
- [51] T. Grafke, R. Grauer, T. Schäfer, and E. Vanden-Eijnden, *Multiscale Modeling & Simulation* **12**, 566 (2014).
- [52] A. Klöckner, N. Pinto, Y. Lee, B. Catanzaro, P. Ivanov, and A. Fasih, *Parallel Computing* **38**, 157 (2012).
- [53] A. J. Robert, *Journal of the Meteorological Society of Japan. Ser. II* **44**, 237 (1966).
- [54] R. Asselin, *Monthly Weather Review* **100**, 487 (1972).
- [55] P. D. Williams, *Monthly Weather Review* **137**, 2538 (2009).
- [56] N. Baddour, *JOSA A* **26**, 1767 (2009).
- [57] I. N. Sneddon, *Fourier transforms* (Courier Corporation, 1995).
- [58] P. Peterson, *International Journal of Computational Science and Engineering* **4**, 296 (2009).